Composites & nanocomposites

Polypyrrole nanotube/ferrocene-modified graphene oxide composites: From fabrication to EMI shielding application

Tengfei Lin[1], Haojie Yu[1,*] (iD), Yun Wang[2], Li Wang[1], Sergey Z. Vatsadze[3], Xiaowei Liu[1], Zhikun Huang[1], Shuning Ren[1], Md Alim Uddin[1], Bilal Ul Amin[1], and Shah Fahad[1]

[1] State Key Laboratory of Chemical Engineering, College of Chemical and Biological Engineering, Zhejiang University, Hangzhou 310027, People's Republic of China

[2] Zhejiang Institute of Mechanical & Electrical Engineering Co., Ltd, Hangzhou 310051, People's Republic of China

[3] N. D. Zelinsky Institute of Organic Chemistry, Russian Academy of Sciences, 47 Leninsky Prosp, Moscow 119991, Russia

ABSTRACT

Polypyrrole nanotube/ferrocene-modified graphene oxide composites (PNT/GO-Fc, PNT/GO-Fc-GO, PNT/GO-EDA-Fc and PNT/GO-EDA-Fc-EDA-GO) were fabricated via *in situ* chemical oxidative polymerization. The prepared composites were characterized by FTIR, XRD, XPS, Raman, TGA, SEM, TEM and EDS. The electromagnetic interference shielding performance of the prepared composites was evaluated by a coaxial method within the frequency range of 1.0–4.5 GHz. The results demonstrated that the composite of PNT/GO-EDA-Fc-EDA-GO-7:1 exhibited the best electromagnetic interference shielding property with 28.73 dB (at the frequency of 1.0175 GHz with the thickness of 3.0 mm) of total shielding effectiveness by adding 50 wt% of the composite in the paraffin matrix. And the composite of PNT/GO-EDA-Fc-EDA-GO-7:1 exhibited good conductivity with a value of 1.320 S/cm. The relationship between the conductivities of prepared samples and the EMI shielding performance was investigated.

Introduction

The rapid development of modern science and technology has brought about convenient wireless communication equipment, navigation systems and electrical equipment [1, 2]; however, the accompanying electromagnetic (EM) pollution cannot be ignored either. EM radiation not only affects the use of precision electronic equipment but also pose a threat to human health [3–5], so the EM pollution problem has aroused people's extensive attention.

Ⓓ Springer

Electromagnetic interference (EMI) shielding materials are commonly used to reduce EM pollution [6, 7]. High EMI shielding performance is achieved mainly by the electrical loss, magnetic loss and multiple reflections loss provided by porous structure, and the electrical loss plays a major role in many systems. Conductive polymer is a typical electrical loss material; moreover, conductive polymer-based composites have become one of the most commonly used EMI shielding materials due to their advantages of good environmental stability and electrical conductivity [8, 9]. Among them, the representative conductive polymer, polypyrrole (PPy), has aroused great interest among researchers due to its high conductivity, environmental stability, easy synthesis and redox properties [10–12]. Nowadays, PPy has been widely used in various fields such as supercapacitors [13], sensors [14], anti-corrosion materials [15], electrode materials [16] and EMI shielding materials [17, 18]. PPy has a variety of micro–nanostructures such as globule, nanowire, nanofiber, nanorod and nanotube [19]. In recent years, polypyrrole nanotube (PNT) has received great attention. Vladimir Babayan et al. [20] reported on the PNT/wood chip composite and tested its shielding effectiveness in the 5.85–8.2 GHz frequency band. The results showed that total shielding effectiveness (SE_T) exceeded 60 dB when the addition amount of PNT was 33 vol.%, which is a very efficient EMI shielding material.

To obtain better conductive properties and mechanical properties at lower conductive polymer additions, scientists usually incorporate conductive polymers with carbon materials such as graphene oxide (GO) [21, 22] and carbon nanotubes (CNTs) [23–26], which possess the properties of large specific surface area, excellent conductivity and mechanical strength. GO is derived from the oxidation of graphene and has a two-dimensional layered structure. The layer contains a large amount of oxygen-containing functional groups such as hydroxyl, epoxy and carboxyl groups, so GO has excellent dispersibility, which is convenient for further processing and modification [27]. GO is used as EMI shielding materials, on whose surface the various oxygen-containing functional groups and defects are conducive to the impedance matching and polarization effect of the composite materials, thereby improving the EMI shielding ability of the composite materials [28].

Ferrocene is a typical organometallic compound and also the earliest found sandwich metallocene complex. Its structure is two parallel cyclopentadiene rings and one Fe atom in the sandwiched position. Similar to aromatic compounds, ferrocene is very stable and can undergo electrophilic substitution reactions, so it can be introduced into other compounds through reactions between functional groups. Ferrocene-modified carbon materials are mainly used in the fields of electrode materials for supercapacitors [29], electrochemical detection [30], sensors [31] and other fields due to their superior redox properties, which are conducive to electron migration. Karthick et al. [32] introduced ferrocene into GO to form nanocomposites through non-covalent modification and tested its electrochemical properties. The results demonstrated that ferrocene molecules had reversible single electron oxidation potential, and the electronic structure of GO could enhance the response current of ferrocene. Gao et al. [33] also studied the non-covalent modification of ferrocene GO. Due to the constraint effect of π–π conjugated system, the thermal stability of intercalated ferrocene compounds was improved, and the sublimation temperature of intercalated ferrocene compounds increased by about 200 K compared with that of the main ferrocene compounds. However, non-covalently modified GO with ferrocene may have problems such as easy removal of ferrocene during the subsequent preparation of composites and processing. The functionalization of GO covalent bond not only improves the dispersion stability of GO lamellas in various solvents, but also improves the compatibility of GO lamellas with polymer matrix. Teimuri-Mofrad et al. [29] grafted GO nanosheets with ferrocene-based compounds by initiating ring-opening polymerization of ferrocene-based ethylene oxide on GO surface. Rabti et al. [34] introduced ferrocene-based carboxylic ester compounds onto the surface of reduced graphene oxide (rGO) by the method of azene chemistry through covalent bonds. Although ferrocene-based compounds can also interact with GO or rGO π–π accumulation through long alkanes of flexible chains, this interaction will be weakened due to the increasing distance in space, thus affecting the electron migration rate in the system. Jin et al. [35] covalently combined small ferrocenylaniline with rGO through –COOH on the surface of rGO. However, the content of –COOH on the surface of rGO is limited, and the

ferrocene-based compounds that can be introduced are limited. Zhou et al. [36] used ethylenediamine to open the ring of the epoxy groups on the GO surface and then reacted ferrocene monoformyl chloride with ethylenediamine modified GO, thus covalently binding the ferrocene groups to GO. However, the improvement of electron migration rate in this system is limited.

The combination of PNT, GO and ferrocene is expected to fabricate good EMI shielding performance materials. Herein, we use active groups such as hydroxyl and epoxy groups on the surface of GO to graft ferrocene as much as possible to form larger π–π stacking systems; it can accelerate electron transfer rate to improve the electrical conductivities of the composite materials, which in turn improves the EMI shielding properties of the composite materials. At the same time, the unused oxygen-containing groups on the surface of GO can retain their dispersibility and facilitate subsequent processing. PNT, due to its unique hollow structure, can improve the multiple reflections part of the composite material against incident EM waves while forming an effective conductive network, thereby further improving the EMI shielding performance of composite materials.

Experimental section

Materials and chemicals

Pyrrole (98%) was purchased from Sigma. Petroleum ether (AR, bp: 60–90 °C), ferric chloride hexahydrate ($FeCl_3 \cdot 6H_2O$, 99%) and oxalyl chloride ($C_2O_2Cl_2$, AR) were purchased from Aladdin chemicals Co. Ltd. Ferrocene monocarboxylic acid (Fc-COOH, AR) and 1,1'-ferrocene dicarboxylic acid (($Fc(COOH)_2$, 98%) were purchased from Beijing Hua Wei Rui Ke Chemical Co. LTD and Saan Chemical Technology (Shanghai) Co. LTD, respectively. Graphene oxide (GO, > 95%) was purchased from Suzhou Carbonfeng Technology Co. LTD. Pyridine (AR), methylene chloride (CH_2Cl_2, AR), triethylamine (TEA, AR), tetrahydrofuran (THF, AR), sodium hydroxide (NaOH, 96.0%), ethylenediamine (EDA, $\geq$ 99.0%) and anhydrous ethanol (C_2H_5OH, $\geq$ 99.7%) were purchased from Sinopharm Co. LTD. Deionized water was laboratory-made. DCM was immersed in 4 Å molecular sieves for 1 week and then refluxed in the presence of CaH_2 for several hours. Pyridine and

TEA were dried with 4 Å molecular sieves for 1 week before use; pyrrole should be distilled at reduced pressure before use. Other chemicals were used as received.

Synthesis of GO-Fc

The ferrocene monoformyl chloride (Fc-COCl) was synthesized according to the literature [37]. The specific operations are as follows: Fc-COOH (10.4099 g, 45.24 mmol) was vacuum-dried at 50 °C in an oil bath for 2 h and set aside under argon protection. In anhydrous and anaerobic conditions, 150.00 mL of refluxed DCM and pyridine (4.70 mL, 58.34 mmol) was injected into the dried Fc-COOH. Then, the excess oxaloyl chloride (5.00 mL, 59.09 mmol) was added with a syringe dropwise, and the reflux reaction was performed at 50 °C for 5 h. After the reaction, the solvent was drained under vacuum, 150.00 mL of petroleum ether was added, and reflux was carried out at 90 °C for 2 h. Then, a spherical sand core funnel was used for closed vacuum filtration, and the solvent petroleum ether was decompressed and drained. After that, Fc-COCl (5.8277 g, 23.45 mmol), 0.6002 g of GO, 60.00 mL of DCM and 4.00 mL (28.86 mmol) of TEA were added and dispersed with ultrasound for 30 min. After the system being dehydrated and deoxygenated, the reaction was performed with stirring at 50 °C for 20 h. Then, GO-Fc was filtered with suction, washed with 150 mL of THF until colorless, rinsed with anhydrous ethanol 2 $\sim$ 3 times, vacuum-dried and placed in a vacuum dryer.

Synthesis of GO-EDA-Fc

0.7014 g of GO, 5.6032 g (139.97 mmol) of NaOH and 350 mL of deionized water were added and sonicated for 1 h. And then, EDA (7.00 mL, 104.83 mmol) was added and reacted at 80 °C for 24 h. After completion of the reaction, it was filtered by suction, washed with 200 mL of deionized water until the pH was neutral, and rinsed with anhydrous ethanol 2 $\sim$ 3 times [38]. Dried Fc-COCl (5.9056 g, 23.76 mmol), 0.3000 g of GO-EDA, TEA (7.00 mL, 50.22 mmol) and 70.00 mL of DCM were added and sonicated for 1 h. After deoxygenation and water removal, the system was placed in an oil bath at 50 °C for 18 h. After the reaction, the solid powder was washed with 150 mL of THF until the filtrate was colorless and then

washed with anhydrous ethanol for 2 ∼ 3 times. The GO-EDA-Fc was obtained after vacuum drying to constant weight.

Synthesis of GO-Fc-GO

The synthesis method of 1,1'-ferrocenedioyl chloride (Fc(COCl)$_2$) is the same as the reference [39], which is as follows. Fc(COOH)$_2$ (11.0330 g, 40.24 mmol) was vacuum-dried at 50 °C for 2 h, and then argon gas was passed into it for storage. 150.00 mL of treated DCM and dehydrated pyridine (9.00 mL, 111.72 mmol) were added. The excess oxalyl chloride (10.00 mL, 118.18 mmol) was added dropwise with a syringe. After heating at 50 °C under reflux for 8 h, the solvent DCM and excess oxalyl chloride were removed in vacuo. One hundred fifty milliliters of dehydrated petroleum ether was added to the reaction flask and refluxed for 2 h. After filtering the suspension in an anhydrous and oxygen-free environment with a spherical sand core funnel, the resulting solution was transferred to a dry flask with a branch, and the solvent and petroleum ether were removed by vacuum. The Fc(COCl)$_2$ (6.1925 g, 19.91 mmol), 0.6008 g of GO, 60.00 mL of DCM and 6.00 mL (43.28 mmol) of TEA were added and sonicated for 30 min and then reacted at 50 °C for 20 h. After the completion of the reaction, it was filtered with suction, washed with 150 mL of THF until colorless and rinsed with anhydrous ethanol 2 ∼ 3 times. The GO-Fc-GO was obtained after vacuum-drying to constant weight.

Synthesis of GO-EDA-Fc-EDA-GO

The Fc(COCl)$_2$ (3.4316 g, 11.04 mmol), 0.3004 g of GO-EDA, 50.00 mL of DCM and 5.00 mL (36.07 mmol) of TEA were added and sonicated for 30 min. After that, the system was dehydrated and oxygen-free and reacted at 50 °C for 20 h. After the reaction, suction filtration was carried out, washed with a 150 mL of THF until colorless and rinsed with anhydrous ethanol several times, and the GO-EDA-Fc-EDA-GO was obtained after vacuum-drying to constant weight.

Preparation of PNT/GO, PNT/GO-Fc, PNT/GO-EDA-Fc, PNT/GO-Fc-GO and PNT/GO-EDA-Fc-EDA-GO composites

The preparation steps of these five composite materials are the same, taking the preparation of PNT/GO-Fc composite as an example. The typical process is as follows[40]: 0.3276 g (1 mmol) of methyl orange was dissolved in 200 mL of deionized water, and then 2.7050 g (10 mmol) of FeCl$_3$·6H$_2$O and 0.1001 g of GO-Fc were added to the above solution. After stirring for 30 min, 0.70 mL of pyrrole monomer was slowly added with a syringe. After stirring the reaction at 25 °C for 24 h, the product was filtered with suction, washed with deionized water and absolute ethanol until the filtrate was colorless, and dried in a vacuum oven at 40 °C to constant weight. For comparison, the preparation method of PNT was the same as that of PNT/carbon material composites, except that the step of adding carbon material was omitted in the preparation process.

Characterization

Scanning electron microscopy (SEM, JEOL-6700F) and transmission electron microscope (TEM, JEOL-1200EX) were employed to observe the morphologies of synthesized samples. Additionally, SEM and TEM instruments are both attached with X-ray energy-dispersive spectrometer (EDS). X-ray diffraction (XRD) pattern was operated on XPert PRO (CuK$_\alpha$, λ = 1.54 Å) X-ray diffractometer. Fourier transform infrared (FTIR) spectroscopy is a method of mixing and tableting with potassium bromide and samples and tested on the Nicolet 5700 infrared spectrometer. Thermogravimetric analysis was performed on a TA-Q500 (Mettler-Toledo) TGA thermogravimetric analyzer, in a nitrogen atmosphere, the heating rate was 10 °C/min, and the temperature range was 50–850 °C. X-ray photoelectron spectroscopy (XPS) spectra were studied on an XPS system of Escalab250Xi. The conductivity test of the samples was carried out on the ST2253 multifunctional digital four-probe tester. The EMI shielding characteristics were measured with an E5071C vector network analyzer (Agilent Technologies). The paraffin and the composite material are uniformly mixed and pressed into a toroidal lamina having an outer diameter of about 7.0 mm, an inner diameter of about 3.04 mm and a thickness of about 3.0 mm.

Results and discussion

Synthesis of modified GO

The synthetic schemes of Fc-COCl, Fc(COCl)$_2$, GO-EDA, GO-Fc, GO-Fc-GO, GO-EDA-Fc and GO-EDA-GO-EDA-Fc are listed in Scheme 1. The experimental synthetic details of Fc-COCl and Fc(COCl)$_2$ are listed in Table 1, and detailed synthetic conditions of GO-EDA, GO-Fc, GO-Fc-GO, GO-EDA-Fc and GO-EDA-Fc-EDA-GO are listed in Tables 2 and 3.

Figure 1a, b shows the FTIR spectra of GO, GO-Fc, GO-Fc-GO, GO-EDA, GO-EDA-Fc and GO-EDA-Fc-EDA-GO. For GO, 3410 cm^{-1}, 2917 cm^{-1} and 2847 cm^{-1} are attributed to –OH stretching absorption band, –CH$_3$ and –CH$_2$ antisymmetric stretching vibration absorption band, respectively; the band of 1720 cm^{-1} is C=O stretching vibration absorption band, and the in-plane bending deformation

vibration absorption band of C=C and –OH and the stretching vibration absorption band of C–O are 1617 cm^{-1}, 1392 cm^{-1} and 1058 cm^{-1}, respectively. 1452 cm^{-1}, 1133 cm^{-1} and 814 cm^{-1} are the characteristic infrared absorption bands of ferrocene [31, 41]. Among them, 814 cm^{-1} belongs to the C–H stretching vibration absorption band on the ferrocene ring [42]. The characteristic peak of GO-Fc at 1452 cm^{-1} is overlapped with the absorption band of C–O in GO. In Fig. 1b, the characteristic bands of ferrocene also appear in GO-EDA-Fc and GO-EDA-Fc-EDA-GO. Meanwhile, GO-EDA, GO-EDA-Fc and GO-EDA-Fc-EDA-GO showed -NH$_2$ scissoring vibration and the swing out-of-plane vibration mode of N–H near 1796 cm^{-1} and 670 cm^{-1}, respectively [43–45], indicating that some of the -NH$_2$ groups remain in GO-EDA-Fc and GO-EDA-Fc-EDA-GO. For GO-EDA, the weak band at 1660 cm^{-1} belongs to the bending vibration of N–H [43]. In GO-EDA-Fc
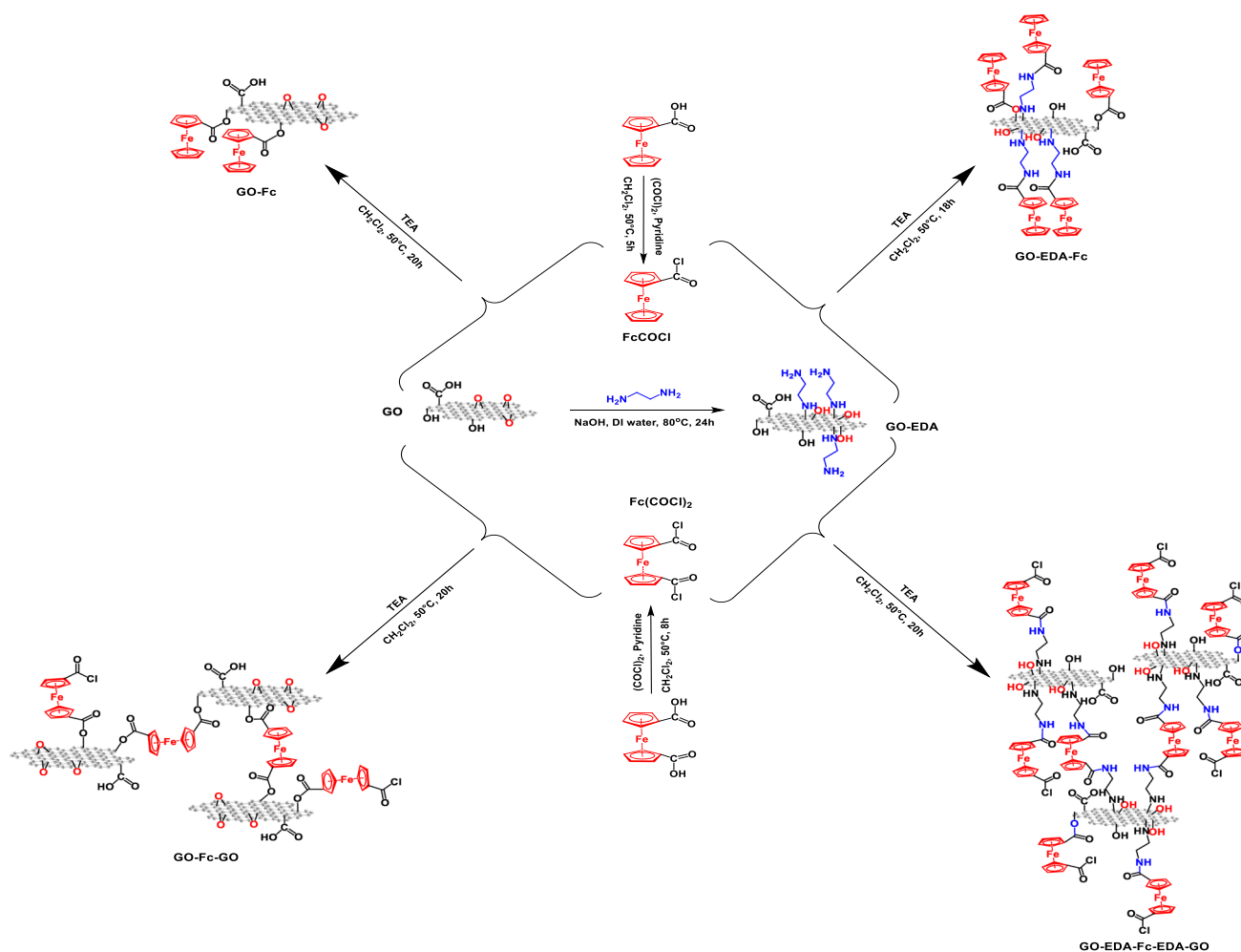
Scheme 1 Synthetic routes for Fc-COCl, Fc(COCl)$_2$, GO-EDA, GO-Fc, GO-EDA-Fc, GO-Fc-GO and GO-EDA-GO-EDA-Fc.

Table 1 Experimental synthetic details for the synthesis of Fc-COCl and Fc(COCl)$_2$

Compound	Step 1					Step 2		Mole ratio	Time	Temperature
	Acid (A)		Pyridine		CH$_2$Cl$_2$	(COCl)$_2$ (B)				
	g	mmol	mL	mmol	mL	mL	mmol	A:B	h	°C
Fc-COCl	10.4099	45.24	4.70	58.34	150.00	5.00	59.09	1:1.31	5	50
Fc(COCl)$_2$	11.0330	40.24	9.00	111.72	150.00	10.00	118.18	1:2.94	8	50

Table 2 Detailed synthetic conditions for the synthesis of GO-EDA

Compound	Step 1					Step 2		Time	Temperature
	NaOH		GO	DI water	$t_{ultrasonic}$	EDA			
	g	mmol	g	mL	h	mL	mmol	h	°C
GO-EDA	5.6032	139.97	0.7014	350	1	7.00	104.83	24	80

Table 3 Detailed synthetic conditions for the synthesis of GO-Fc, GO-Fc-GO, GO-EDA-Fc and GO-EDA-Fc-EDA-GO

Compound	Step 1				Step 2		Time	Temperature
	GO or GO-EDA	TEA		CH$_2$Cl$_2$	FcCOCl or Fc(COCl)$_2$			
	g	mL	mmol	mL	g	mmol	h	°C
GO-Fc	[a]0.6002	4.00	28.86	60.00	[c]5.8277	23.45	20	50
GO-Fc-GO	[a]0.6008	6.00	43.28	60.00	[d]6.1925	19.91	20	50
GO-EDA-Fc	[b]0.3000	7.00	50.22	70.00	[c]5.9056	23.76	18	50
GO-EDA-Fc-EDA-GO	[b]0.3004	5.00	36.07	50.00	[d]3.4316	11.04	20	50

[a]GO, [b]GO-EDA, [c]FcCOCl, [d]Fc(COCl)$_2$
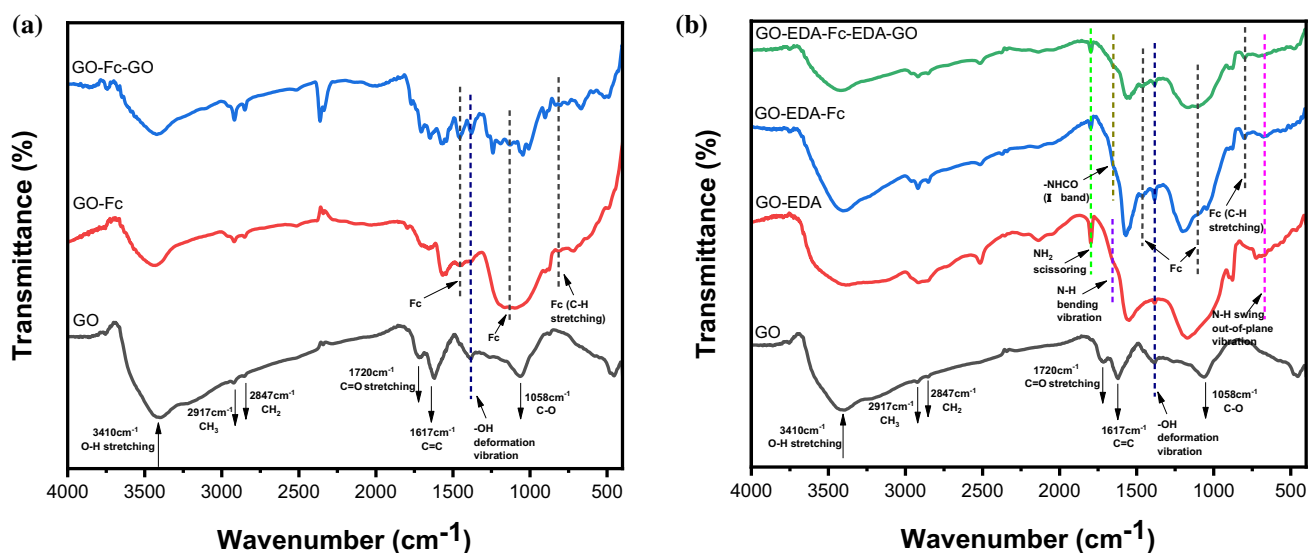
Figure 1 FTIR spectra of GO and (**a**) GO-Fc and GO-Fc-GO, (**b**) GO-EDA, GO-EDA-Fc and GO-EDA-Fc-EDA-GO.

and GO-EDA-Fc-EDA-GO, the weak band of 1660 cm^{-1} is the characteristic absorption band of the amide I band, while the characteristic absorption band of the amide II band is masked by the broad band of GO's aromatic ring skeleton vibration [46].

Figure 2a, b shows the XRD patterns of GO, GO-Fc, GO-Fc-GO, GO-EDA, GO-EDA-Fc and GO-EDA-Fc-EDA-GO. It can be seen that GO at $2\theta = 28.2°$ and $42.4°$ correspond to (002) and (111) crystal planes of graphite structure, respectively, and the sharp characteristic diffraction peak at $2\theta = 12.2°$ corresponds to (100) crystal plane of GO [47–49]. For the GO-Fc in Fig. 2a, the (100) crystal plane becomes broad peaks with lower diffraction intensity and shifts to a low diffraction angle $2\theta = 10.8°$, which indicates that the successful modification of ferrocene groups makes the distance larger between GO. The broad

diffraction peak of $2\theta = 13.2–22.4°$ belongs to the ferrocene modified by GO surface. The diffraction intensity of GO-Fc-GO and (100) crystal plane in Fig. 2a is lower than that of GO-Fc, and it is further shifted to a low diffraction angle $2\theta = 8.2°$, which indicates that 1,1'-ferrocene group-modified GO further increases the distance between GO, and in the XRD spectrum of GO-Fc-GO, a broad peak of $2\theta = 12–20°$ attributed to ferrocene also appears. Meanwhile, both GO-Fc and GO-Fc-GO also have a graphite-structure (111) crystal plane at $2\theta = 42.4°$, but the intensity is decreased compared to pure GO. In Fig. 2b, when the epoxy groups on the GO surface are opened with ethylenediamine (GO-EDA), there is a broad diffraction peak at $2\theta = 16–30°$, and the (100) crystal plane of GO becomes a much lower diffraction intensity broad peak. The XRD patterns of GO-EDA-
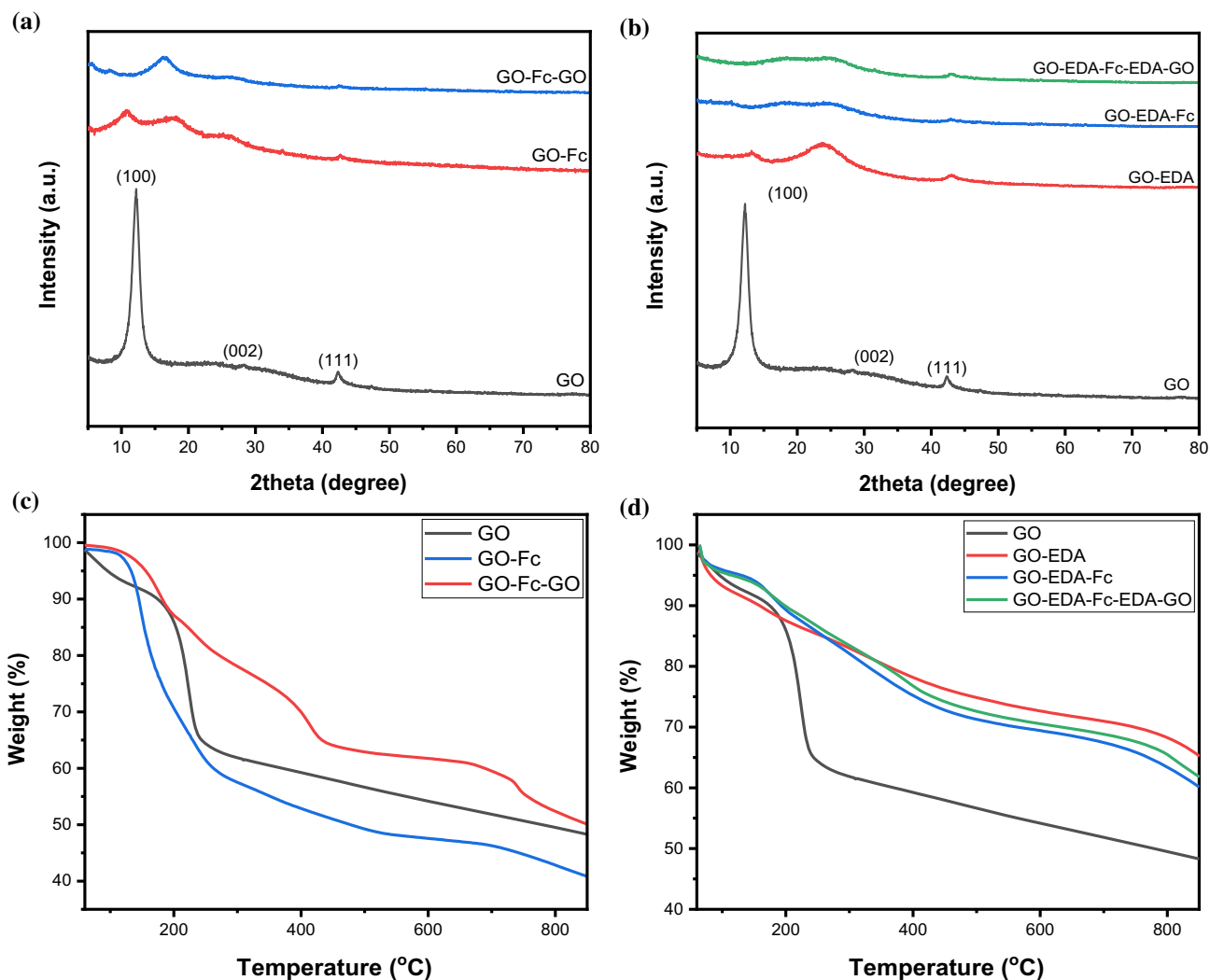

Figure 2 XRD patterns (**a**, **b**) and TGA curves (**c**, **d**) of GO, GO-Fc, GO-Fc-GO, GO-EDA, GO-EDA-Fc and GO-EDA-Fc-EDA-GO.

Fc and GO-EDA-Fc-EDA-GO have little difference. The wide peak at $2\theta = 12–30°$ is the result of the modification of ethylenediamine and ferrocene. Both GO-EDA-Fc and GO-EDA-Fc-EDA-GO have graphite-structure (111) crystal faces at $2\theta = 42.4°$, but the intensity is lower than that of GO. The above analysis of XRD patterns also prove the successful preparation of GO-Fc, GO-Fc-GO, GO-EDA, GO-EDA-Fc and GO-EDA-Fc-EDA-GO. Figure 2c, d shows the TGA curves of GO, GO-Fc, GO-Fc-GO, GO-EDA, GO-EDA-Fc and GO-EDA-Fc-EDA-GO. For unmodified GO, the main weightlessness temperature range is 150–300 °C, which is mainly due to the CO, CO_2 and steam generated by the pyrolysis of unstable oxygen-containing functional groups; Slower mass loss can be observed at 300–850 °C, which might be attributed to the removal of more stable oxygen-containing functional groups [48, 50, 51]. It can be seen from Fig. 2c, d that all the thermal stability of modified GO has been significantly improved except GO-Fc.

To determine the interactions between GO and surface modification groups, Raman spectroscopy was further employed. Figure 3 shows the Raman spectra of GO, GO-Fc, GO-Fc-GO, GO-EDA, GO-EDA-Fc and GO-EDA-Fc-EDA-GO. The G band is generated by the stretching of the sp^2 hybrid carbon atoms, indicating the degree of order of the graphite structure; and the D band reflects the defects of the graphite internal structure, which is the sp^2 hybridized carbon atoms caused by breathing vibration
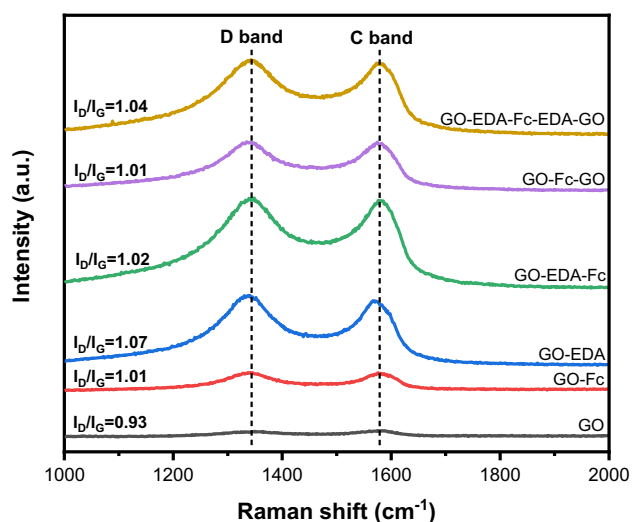
[52]. The I_D/I_G ratio indicates the disorder degree of graphite, the larger the ratio, the greater the disorder degree and the more defects [48, 52]. It can be seen from Table 4 that the I_D/I_G of unmodified GO is 0.93, which is consistent with the value in the literature [53]. The modified GO has a larger I_D/I_G ratio than original GO, which shows that the modified GO is more disordered and has more defects, indicating that sp^3 hybridized carbon atoms are formed during the functionalization process [54]. Compared with original GO, the positions of D band and G band also have a certain degree of red-shift or blue-shift, this might be due to the chemical bond between the carbon atoms of GO and functional groups that interfere with the surface structure of GO [55], which further proves that successfully modification.

To further explore the elemental composition, bonding type and chemical valence of the samples, the XPS test was performed on GO, GO-Fc, GO-Fc-GO, GO-EDA, GO-EDA-Fc and GO-EDA-Fc-EDA-GO, and the XPS spectra are shown in Fig. 4 and Fig. S4. In the C1s spectrum, the electron binding energies of 282.9 eV, 283.4 eV, 283.9 eV, 285.2 eV and 287.0 eV correspond to C–C, C–OH, C=O, C=O and O–C=O, respectively [56]. In the O1s spectrum, O–C=O, C=O, C–OH and C–O–C peaks are at 530.1 eV, 531.1 eV, 531.9 eV and 532.2 eV, respectively [57]. For the N1s spectrum, 398.5 eV and 401.3 eV correspond to N–H and C–N, respectively [58]. From Fig. 4a–c and Fig. S4a–h, it can be seen that compared to the original GO (Fig. 4c), the modified GO, GO-Fc and GO-Fc-GO (Fig. S4c, Fig. S4g), the C–OH content on the surface was significantly reduced, which is consistent with the introduction of ferrocene through hydroxyl groups. The wide scan showed that all samples contain C and O elements, and N elements were all present in GO-EDA, GO-EDA-Fc and GO-EDA-Fc-EDA-GO, which indicated that ethylenediamine had successfully modified on GO. Furthermore, GO-Fc, CO-Fc-GO, GO-EDA-Fc and CO-EDA-Fc-EDA-GO all contained Fe, which further illustrated the successful introduction of ferrocene. In the Fe2p spectrum, 706.6 eV, 710.0 eV, 719.3 eV and 724.2 eV correspond to Fe(II) 2p3/2, Fe(III) 2p3/2, Fe(II) 2p1/2 and Fe(III) 2p1/2, respectively. From Fig. 4h, Fig. S4d, Fig. S4h and Fig. S4m, it can be seen that the Fe element was mainly Fe(II), and a small amount of Fe(III) may be due to the oxidation of part of the ferrocene [59]. To observe the morphologies and structures of the prepared samples, SEM

Figure 3 Raman spectra of GO, GO-Fc, GO-EDA, GO-Fc-GO, GO-EDA-Fc and GO-EDA-Fc-EDA-GO.

Table 4 Raman detail data of GO, GO-Fc, GO-EDA, GO-Fc-GO, GO-EDA-Fc and GO-EDA-Fc-EDA-GO

Sample	I_D	Raman shift (cm^{-1})	I_G	Raman shift (cm^{-1})	I_D/I_G
GO	440	1350.13	472	1574.68	0.93
GO-Fc	1114	1337.39	1102	1576.23	1.01
GO-EDA	3616	1337.5	3378	1567.04	1.07
GO-EDA-Fc	4816	1348.65	4712	1576.33	1.02
GO-Fc-GO	2622	1334.31	2608	1574.78	1.01
GO-EDA-Fc-EDA-GO	4034	1342.28	3880	1573.24	1.04
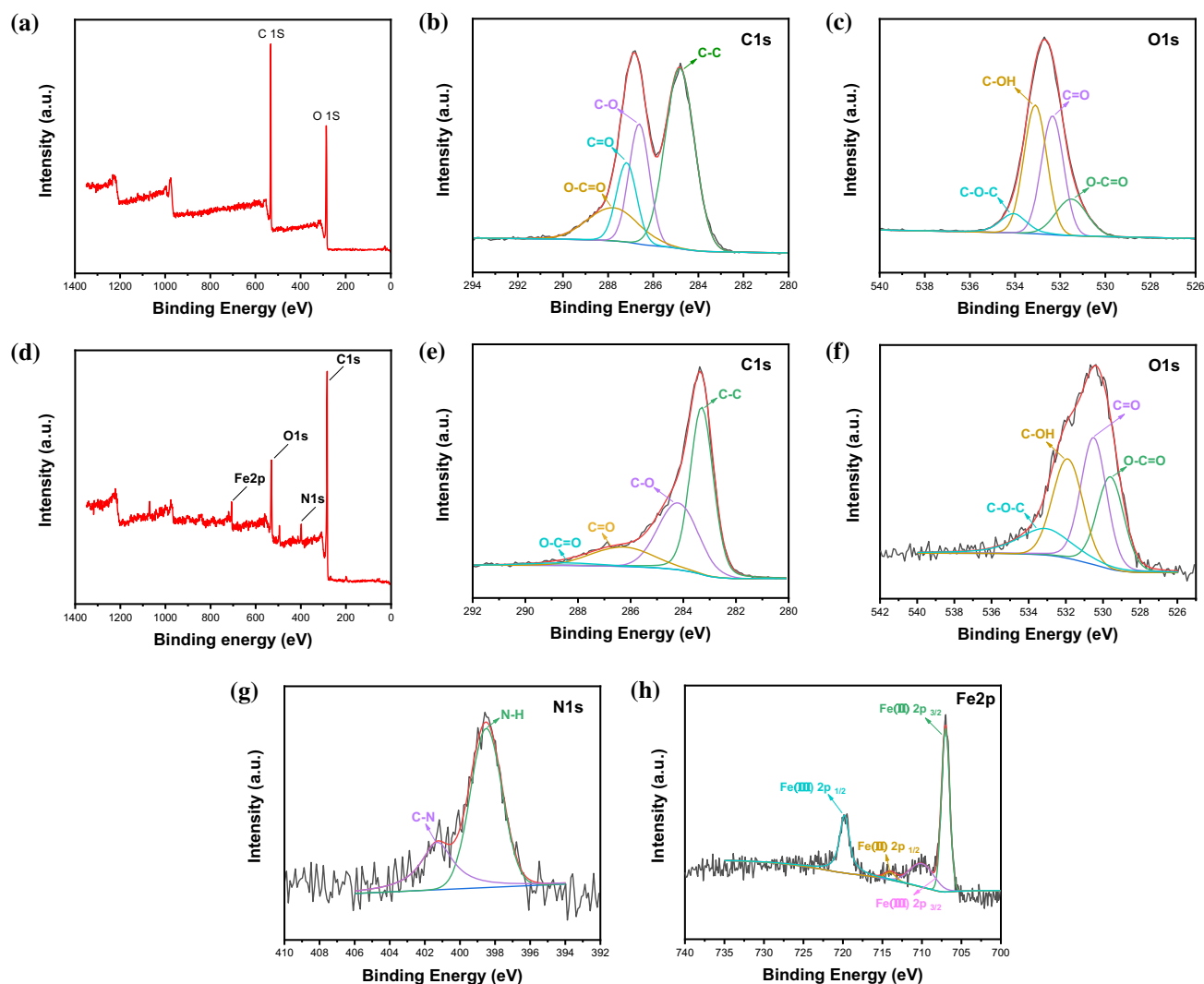
Figure 4 XPS **a** wide scan, **b** C1s, **c** O1s spectra of GO and **d** wide scan, **e** C1s, **f** O1s, **g** N1S, **h** Fe2p spectra of GO-EDA-Fc-EDA-GO.

equipment was first employed. Fig. S1 are the SEM images of pristine GO and modified GO. It can be seen from Fig. S1a that compared to the modified GO, the surface of pristine GO was relatively smoother with some visible wrinkles. Figure S1b–f corresponds to the samples of GO-Fc, GO-Fc-GO, GO-EDA, GO-EDA-Fc and GO-EDA-Fc-EDA-GO, respectively. The

modified GO had a rougher surface with amounts of protrusions and wrinkles. Figure S2 shows the TEM images of the pristine GO and the modified GO. From Fig. S2a, it can be seen that the pristine GO was thin and transparent with obvious wrinkles. Figure S2b-f shows the TEM images of GO-Fc, GO-Fc-GO, GO-EDA, GO-EDA-Fc and GO-EDA-Fc-EDA-GO,

respectively. GO-Fc-GO (Fig. S2c), GO-EDA-Fc (Fig. S2e) and GO-EDA-Fc-EDA-GO (Fig. S2f) were thicker than the pristine GO, and there were fewer wrinkles on the surface, especially the sample GO-EDA-Fc-EDA-GO, which is also mutually corroborated with its formula in Scheme 1. The reason is that 1,1′-ferrocene dicarboxylic acid chloride connected multiple GO sheets to result in the formation of a larger π–π stacking system so that the modified GO sheet became more, and the TEM image presented a thick and less wrinkled morphology.

Preparation and characterization of PNT, PNT/GO and PNT/modified GO

Figure 5 shows the FTIR spectra of PNT, PNT/GO, PNT/GO-Fc, PNT/GO-Fc-GO, PNT/GO-EDA-Fc and PNT/GO-EDA-Fc-EDA-GO-7:1. For pure PNT (Fig. 5a), 1544 cm^{-1} and 1459 cm^{-1} are the classical vibrations of the pyrrole ring, which belong to the C–C and the C–N stretching vibration of the pyrrole ring, respectively. 1312 cm^{-1}, 1172 cm^{-1}, 1097 cm^{-1} and 1037 cm^{-1} correspond to the in-plane bending vibration of C–H or C–N, the breathing vibration band of the pyrrole ring, the N^+–H vibration band and the hydrocarbon vibration band in the plane, respectively. The C–C out-of-plane vibration, N–H swing and N–H out-of-plane vibration band are at 967 cm^{-1}, 902 cm^{-1} and 782 cm^{-1}, respectively [60–62]. Compared with the original GO, the infrared
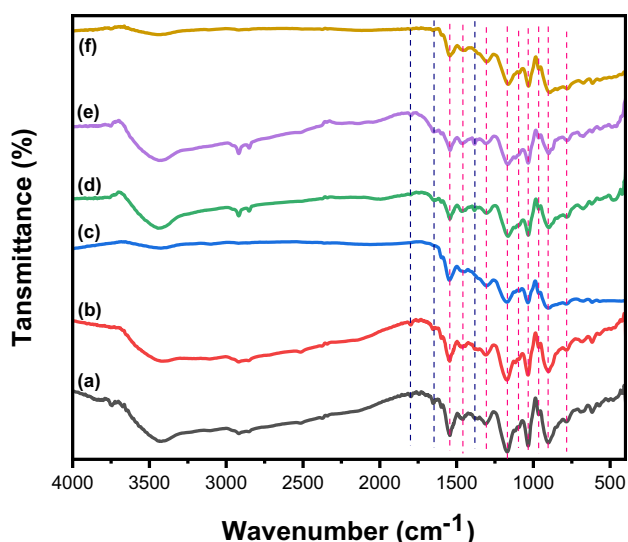

Figure 5 FTIR of **a** PNT, **b** PNT/GO, **c** PNT/GO-Fc, **d** PNT/GO-Fc-GO, **e** PNT/GO-EDA-Fc and **f** PNT/GO-EDA-Fc-EDA-GO-7:1.

characteristic band of GO in the composite material has a certain red-shift or blue shift due to the interaction with PNT. 1800 cm^{-1}, 1651 cm^{-1} and 1387 cm^{-1} correspond to the C=O stretching vibration absorption band, the C=C and –OH in-plane bending deformation vibration absorption band, respectively. The stretching vibration absorption band of C–O and several characteristic absorption bands of ferrocene overlap with the infrared band of PNT. Figure 6 describes the schematical diagram of the preparation process of PNT integrated with GO-EDA-Fc and GO-EDA-Fc-EDA-GO, respectively. The detailed preparation conditions of composites are listed in Table 5.

Figure 7a–f shows the SEM images of PNT, PNT/GO, PNT/GO-Fc, PNT/GO-Fc-GO, PNT/GO-EDA-Fc and PNT/GO-EDA-Fc-EDA-GO-7:1, respectively. It can be observed from the SEM images that the PNT was a rod-shaped structure with a length of about ten microns and a diameter of several hundred nanometers, and the composite materials PNT/GO, PNT/GO-Fc and PNT/GO-Fc-GO lamellar structures with different morphologies appeared in all of the images, which further illustrated the successful integration of PNT with original GO and modified GO.

Figure 8 and Fig. S5 show TEM images of composite materials PNT/GO, PNT/GO-Fc, PNT/GO-Fc-GO, PNT/GO-EDA-Fc and PNT/GO-EDA-Fc-EDA-GO-7:1 and the corresponding TEM-EDS mapping images. The hollow structure of PNT can be seen in the TEM images of all five samples. The TEM-EDS mapping images showed that all samples contain C, O and N elements, and PNT/GO-Fc, PNT/GO-Fc-GO, PNT/GO-EDA-Fc and PNT/GO-EDA-Fc-EDA-GO-7:1 also contained Fe element, which indicated the successful introduction of the ferrocene groups. The N element contained in PNT/GO, PNT/GO-Fc and PNT/GO-Fc-GO only came from PNT, while the mapping diagram showed that both the original GO and the modified GO contain a large amount of N element, this is because part of the pyrrole monomer in the reaction process was adsorbed on the surface of the flake GO, GO-Fc and GO-Fc-GO with large specific surface area, and polypyrrole was formed *in situ* under the action of the oxidant. Part of the N element contained in PNT/GO-EDA-Fc and PNT/GO-EDA-Fc-EDA-GO-7:1 came from PNT, and the other part came from the modification of GO by ethylenediamine.
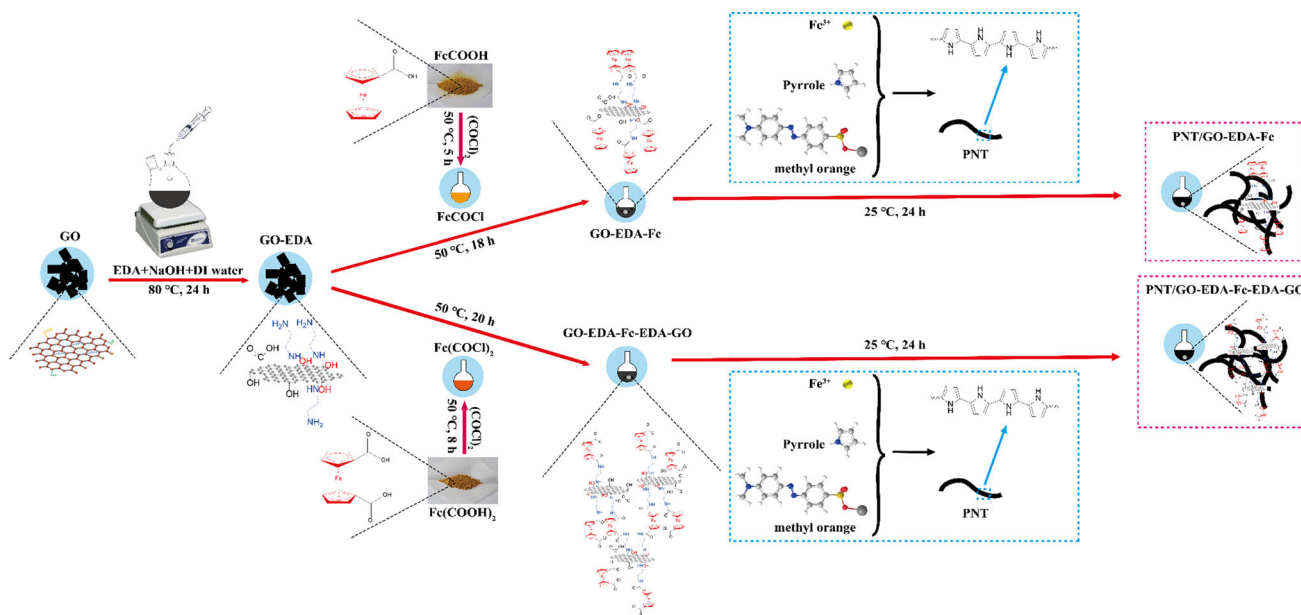
Figure 6 Schematical diagram of the preparation process of PNT/GO-EDA-Fc and PNT/GO-EDA-Fc-EDA-GO composites.

Table 5 Experimental details for the preparation of PNT, PNT/GO, PNT/GO-Fc, PNT/GO-Fc-GO, PNT/GO-EDA-Fc and PNT/GO-EDA-Fc-EDA-GO-7:1

Sample	Step 1		Step 2			Step 3	Time	Temperature
	MO g/mmol	DI water mL	FeCl$_3$·6H$_2$O g/mmol	GO or modified GO g	t$_{stir}$ h	Py mL/mmol	h	°C
PNT	0.3269/1.0	200	2.7069/10.0	0	0.5	0.70/10.1	24	25
PNT/GO	0.3269/1.0	200	2.7053/10.0	0.1008	0.5	0.70/10.1	24	25
PNT/GO-Fc	0.3276/1.0	200	2.7050/10.0	[a]0.1001	0.5	0.70/10.1	24	25
PNT/GO-Fc-GO	0.3268/1.0	200	2.7066/10.0	[b]0.1002	0.5	0.70/10.1	24	25
PNT/GO-EDA-Fc	0.3274/1.0	200	2.7031/10.0	[c]0.1003	0.5	0.70/10.1	24	25
PNT/GO-EDA-Fc-EDA-GO-7:1	0.3272/1.0	200	2.7067/10.0	[d]0.1008	0.5	0.70/10.1	24	25

[a]GO-Fc, [b]GO-Fc-GO, [c]GO-EDA-Fc, [d]GO-EDA-Fc-EDA-GO

Figure S3 shows the TGA curves of PNT, PNT/GO, PNT/GO-Fc, PNT/GO-Fc-GO, PNT/GO-EDA-Fc and PNT/GO-EDA-Fc-EDA-GO-7:1. It can be seen that the TG curves of the composite materials were not much different from that of the polymer, and the thermal stability was only slightly improved. This may be due to the small amount of carbon material was added to the composite materials. And the final quality of the residual rate was around 50%.

Conductivity and EMI shielding performance

To investigate the influence of electrical conductivity on the performance of EMI shielding, the resistance of the composite material was measured by the four-

Figure 7 SEM images of
a PNT, **b** PNT/GO, **c** PNT/
GO-Fc, **d** PNT/GO-Fc-GO,
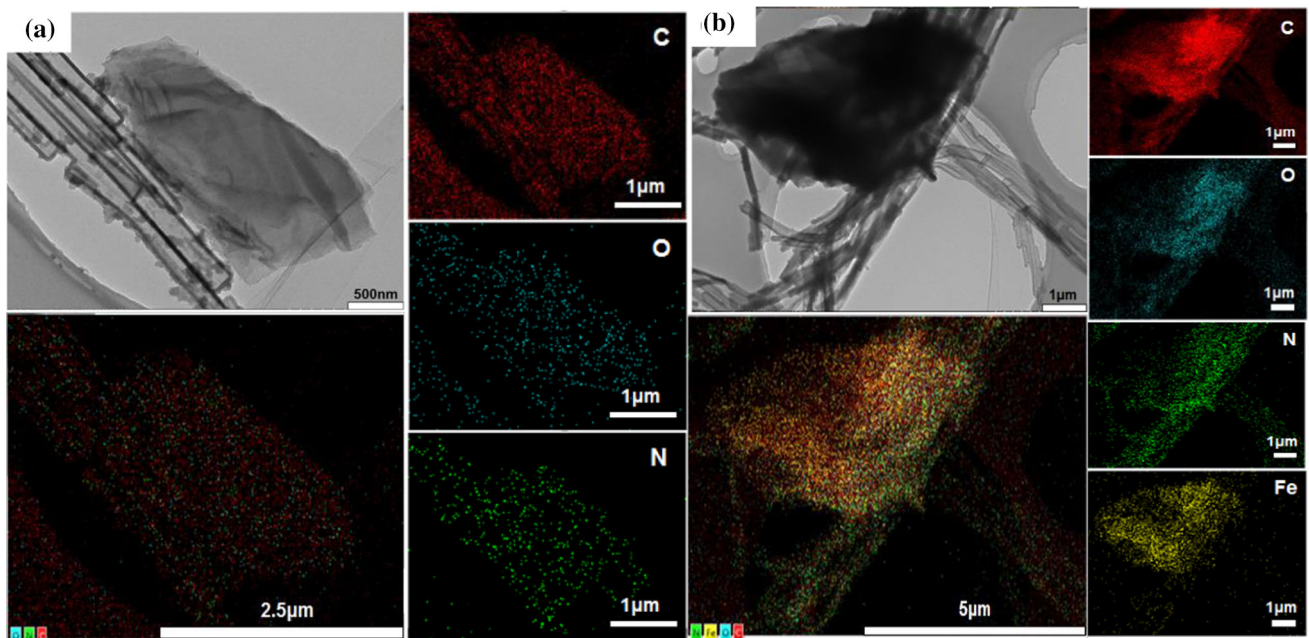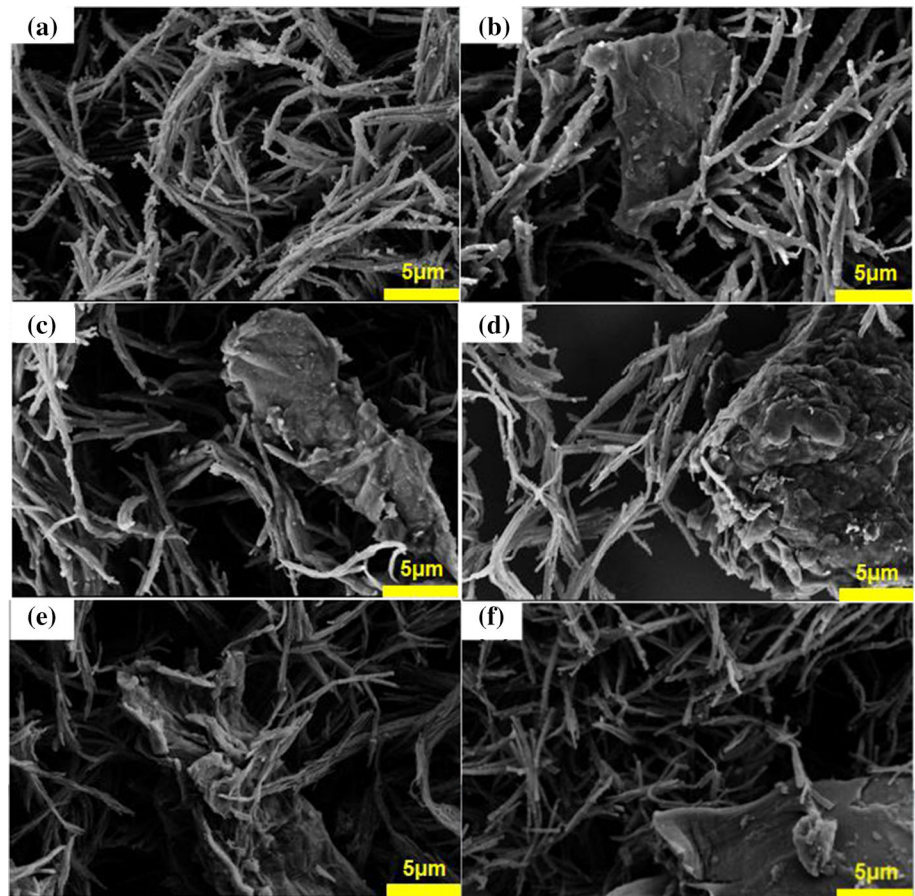**e** PNT/GO-EDA-Fc and
f PNT/GO-EDA-Fc-EDA-GO-
7:1.

Figure 8 TEM images and corresponding TEM-EDS mapping of **a** PNT/GO and **b** PNT/GO-EDA-Fc-EDA-GO-7:1 for the selected image.

probe method. The procedure for preparing a test sample for electrical conductivity is as follows: 45 mg of composite material and 5 mg of polyvinylidene fluoride (PVDF) powder are comminuted to a soft powder and pressed into a circular sheet of compressed tablets (pressure 10 MPa). To reduce the test error, 3 points were measured and averaged for each sample. Table 6 shows a summary of conductivity values. EM interference shielding effectiveness (EMI SE) is often employed to evaluate the performance of EMI shielding materials. There is no doubt that the total EMI SE (SE_{total}) is the sum of the absorption (SE_A), reflectance (SE_R) and internal multiple reflections (SE_M) [63]. And SE_M can be omitted if SE_{total} > 10 dB [64]. The calculations are based on equations below [65–67], where S_{11} and S_{21} are the tested S parameters.

$$SE_{total} = SE_R + SE_A \qquad (1)$$

$$SE_A = 10\lg\frac{1-R}{T} \qquad (2)$$

$$SE_R = 10\lg\frac{1}{1-R} \qquad (3)$$

$$R = \frac{P_r}{P_i} = |S_{11}|^2 \qquad (4)$$

$$T = \frac{P_t}{P_i} = |S_{21}|^2 \qquad (5)$$

To investigate the relationship between the composite material and its EMI shielding performance, Eqs. (6), (7) and (8) can be used instead of Eqs. (2), (3) and (1), respectively [68]:

$$SE_A = 8.7d\sqrt{\pi f\mu\sigma} \qquad (6)$$

$$SE_R = 39.5 + 10\lg\frac{\sigma}{2\pi f\mu} \qquad (7)$$

$$SE_{total} = SE_A + SE_R = 8.7d\sqrt{\pi f\mu\sigma} + 39.5 + 10\lg\frac{\sigma}{2\pi f\mu} \qquad (8)$$

In the above equations, σ, μ and d are the conductivity, permeability and the thickness of the EMI shielding material, respectively. f is the frequency of EM wave. According to Eqs. (6), (7) and (8), the conductivity is positively correlated with SE_{total}, SE_A and SE_R.

Figure 9 shows the EMI SE, conductivity, SE_T, SE_A, SE_R, A, R and T graphs of GO, GO-Fc, GO-Fc-GO, GO-EDA-Fc and GO-EDA-Fc-EDA-GO. As can be seen from Fig. 9a, the EMI SE of GO-Fc-GO modified by the ferrocene groups was similar to that of GO, and the trend of the scatter diagram is almost the same. This can also be confirmed by the conductivity results shown in Fig. 9b; GO and GO-Fc-GO had similar conductivity, only 7.813×10^{-5} S/cm and 1.204×10^{-4} S/cm, respectively. However, the EMI SE value of GO modified by ferrocene groups (GO-Fc) was significantly improved, and its conductivity was more than twice that of GO-Fc-GO, reaching 2.766×10^{-4} S/cm. The EMI shielding performance of ethylenediamine-functionalized GO modified by ferrocene groups (GO-EDA-Fc) and ferrocene group-functionalized GO (GO-EDA-Fc-EDA-GO) was significantly improved compared with that of original GO. The conductivity results in Fig. 9b are also

Table 6 Summary of conductivity values

| Sample	Conductivity (S/cm)				Standard deviation
	1	2	3	Mean	
GO	7.883×10^{-5}	7.810×10^{-5}	7.748×10^{-5}	7.813×10^{-5}	6.751×10^{-7}
GO-Fc	2.822×10^{-4}	2.717×10^{-4}	2.760×10^{-4}	2.766×10^{-4}	5.280×10^{-6}
GO-Fc-GO	1.192×10^{-4}	1.202×10^{-4}	1.217×10^{-4}	1.204×10^{-4}	1.255×10^{-6}
GO-EDA-Fc	2.570×10^{-3}	2.560×10^{-3}	2.460×10^{-3}	2.530×10^{-3}	5.748×10^{-5}
GO-EDA-Fc-EDA-GO	1.033×10^{-2}	1.012×10^{-2}	9.670×10^{-3}	1.004×10^{-2}	3.377×10^{-4}
PNT	5.165×10^{-1}	4.975×10^{-1}	5.101×10^{-1}	5.080×10^{-1}	9.670×10^{-3}
PNT/GO	7.547×10^{-2}	7.543×10^{-2}	7.382×10^{-2}	7.491×10^{-2}	9.413×10^{-4}
PNT/GO-Fc	5.212×10^{-1}	5.410×10^{-1}	5.245×10^{-1}	5.289×10^{-1}	1.061×10^{-2}
PNT/GO-Fc-GO	3.595×10^{-1}	3.540×10^{-1}	3.576×10^{-1}	3.570×10^{-1}	2.790×10^{-3}
PNT/GO-EDA-Fc	1.774×10^{-1}	1.655×10^{-1}	1.677×10^{-1}	1.702×10^{-1}	6.330×10^{-3}
PNT/GO-EDA-Fc-EDA-GO-7:1	1.329×10^{0}	1.277×10^{0}	1.354×10^{0}	1.320×10^{0}	3.904×10^{-2}
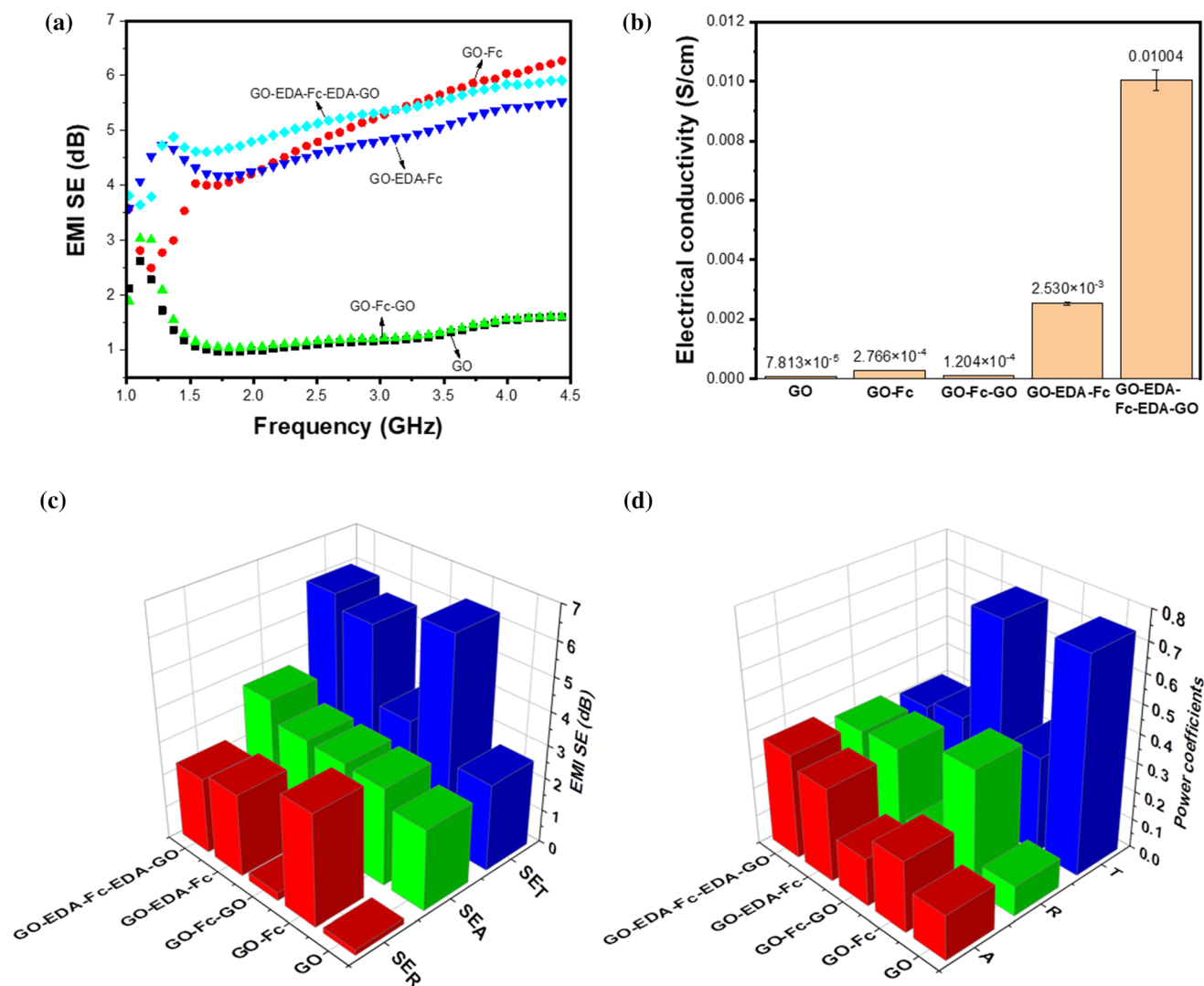
Figure 9 The **a** EMI SE, **b** conductivity, **c** SE_T, SE_A, SE_R and **d** A, R, T of GO, GO-Fc, GO-Fc-GO, GO-EDA-Fc and GO-EDA-Fc-EDA-GO.

consistent with the EMI shielding performance for the unmodified GO; the conductivity was only 7.813×10^{-5} S/cm [69]. The conductivity of GO-EDA-Fc was improved by nearly two orders of magnitude, reaching 2.530×10^{-3} S/cm, and the conductivity of GO-EDA-Fc-EDA-GO even reached 1.004×10^{-2} S/cm. This is also consistent with the experimental idea designed. Through the introduction of ferrocene groups, a larger π–π stacking interaction system was formed, which accelerated the electron transfer rate and thus improved its EMI shielding performance. From the SE_T, SE_A and SE_R diagrams in Fig. 9c, we can see that the SE_A of all five samples were similar, but the reflected EMI shielding effectiveness (SE_R) of GO-Fc was the largest; that is, the reflection loss of

GO-Fc was the largest, reaching 6.33 dB. The SE_R of GO and GO-Fc-GO was very low, indicating that most of the EM waves entering the shielding material were mainly absorption loss. The SE_A and SE_R values are based on EM waves penetrating into the material, excluding reflected waves. Unlike SE_R and SE_A, R and A represent the absolute values of the reflected and absorbed powers, respectively [70]. Because of the easy occurrence of reflection, when EM waves are projected on the surface of the material, few EM waves enter the inside of the shielding material, so the absorption performance of the shielding material is not fully utilized. Therefore, the shielding material may have a high R value but a low SE_R value, or a low A value but a high SE_A value [71]. The power

coefficients A, R and T measured in the frequency range of 1.0–4.5 GHz are demonstrated in Fig. 9d. It can be seen from the figure that compared with other samples, the A and R of GO and GO-Fc-GO were lower, making the value of T higher. The EMI shielding performance of GO and modified GO samples were not merely based on reflection or absorption as the main mechanism, but the result of the combined effect of reflection and absorption. After the introduction of EDA, the amide groups (–CO–NH–) are easier to form hydrogen bonds than the ester groups (–COO–), which increases the interaction force between molecules and between PNT, so as to facilitate charge transfer, thus making the performance of samples with EDA (GO-EDA-Fc and GO-EDA-Fc-EDA-GO in Scheme 1) were better than those without EDA (GO-Fc and GO-Fc-GO in Scheme 1).

Figure 10 corresponds to EMI SE, conductivity, SE_T, SE_A, SE_R, A, R and T graphs of PNT, PNT/GO, PNT/GO-Fc-GO, PNT/GO-Fc-GO, PNT/GO-EDA-Fc and PNT/GO-EDA-Fc-EDA-GO-7:1. As can be seen from Fig. 10a, EMI SE of PNT/GO-Fc and PNT/GO-Fc-GO was slightly improved compared with PNT, reaching 19.9 dB and 20.8 dB, respectively, while PNT/GO was only 11.7 dB. This situation is similar to the conductivity test results in Fig. 10b. The conductivity of PNT/GO was only 7.491×10^{-2} S/cm, while the conductivities of PNT, PNT/GO-Fc and PNT/GO-Fc-GO were relatively high, reaching 5.080×10^{-1} S/cm, 5.289×10^{-1} S/cm and 3.570×10^{-1} S/cm, respectively. Although the conductivity of PNT/GO-Fc-GO was lower than that of PNT, the EMI SE value of PNT/GO-Fc-GO was even higher than that of PNT, indicating that the EMI shielding performance in this system did not only depend on its conductivity, but the microstructure of the material could affect its dissipation of incident EM wave to a certain extent. And the influence of microstructure may be due to the stronger interfacial polarization effect generated by the heterogeneous interface formed between PNT and GO-Fc-GO, so as to obtain better EMI shielding performance. The EMI shielding performance of PNT/GO-EDA-Fc-EDA-GO was better than others, its EMI SE value was as high as 28.7 dB, while the SE_T of PNT/GO-EDA-Fc was only 15.6 dB, even lower than the 19.8 dB of

PNT, which was completely consistent with the test results of conductivity. The conductivity of PNT/GO-EDA-Fc was 1.702×10^{-1} S/cm, far lower than the 5.080×10^{-1} S/cm of PNT, while the conductivity of PNT/GO-EDA-Fc-EDA-GO-7:1 was as high as 1.320 S/cm. It can be seen from Fig. 10c that the SE_R values of PNT, PNT/GO, PNT/GO-Fc, PNT/GO-Fc-GO, PNT/GO-EDA-Fc and PNT/GO-EDA-Fc-EDA-GO-7:1 were similar, but the absorption EMI shielding efficiency (SE_A) of PNT/GO and PNT/GO-EDA-Fc was only half that of the other samples, making their SE_T much lower than that of the other four samples. This may be due to the poor dispersion of corresponding carbon materials in PNT/GO and PNT/GO-EDA-Fc so that the composite materials did not form a good conductive network path, which led to insufficient dissipation of EM waves, thus weakening their EMI shielding performance.

For all of the samples, the values of SE_A were higher than those of SE_R, which illustrated that the EM waves entering the shielding material were mainly absorption loss. Figure 10d demonstrates the power coefficients A, R and T of composite materials measured in the frequency range of 1.0–4.5 GHz. The electrical conductivities of the composite samples were significantly higher than those of carbon materials (Figs. 9b, 10b), and the value of R is closely related to the electrical conductivity[71, 72]; therefore, it can be seen from Fig. 10d that the R values of the composites were high, so mainly part of EM waves were reflected on the surface of shielding composites, and the EM waves transmitted can be almost negligible. Compared with other samples, the R values of PNT/GO and PNT/GO-EDA-Fc were slightly lower, and their SE_T was also lower.

Different fraction ratios of GO-EDA-Fc-EDA-GO on the conductivity and EMI shielding performance

To investigate the influence of different fraction ratios of GO-EDA-Fc-EDA-GO on EMI shielding performance, five groups of experiments shown in Table 7 were performed. According to the feeding mass ratio of reactant pyrrole and, GO-EDA-Fc-EDA-GO, the samples were named as PNT/GO-EDA-Fc-EDA-GO-3:1, PNT/GO-EDA-Fc-EDA-GO-5:1, PNT/GO-EDA-
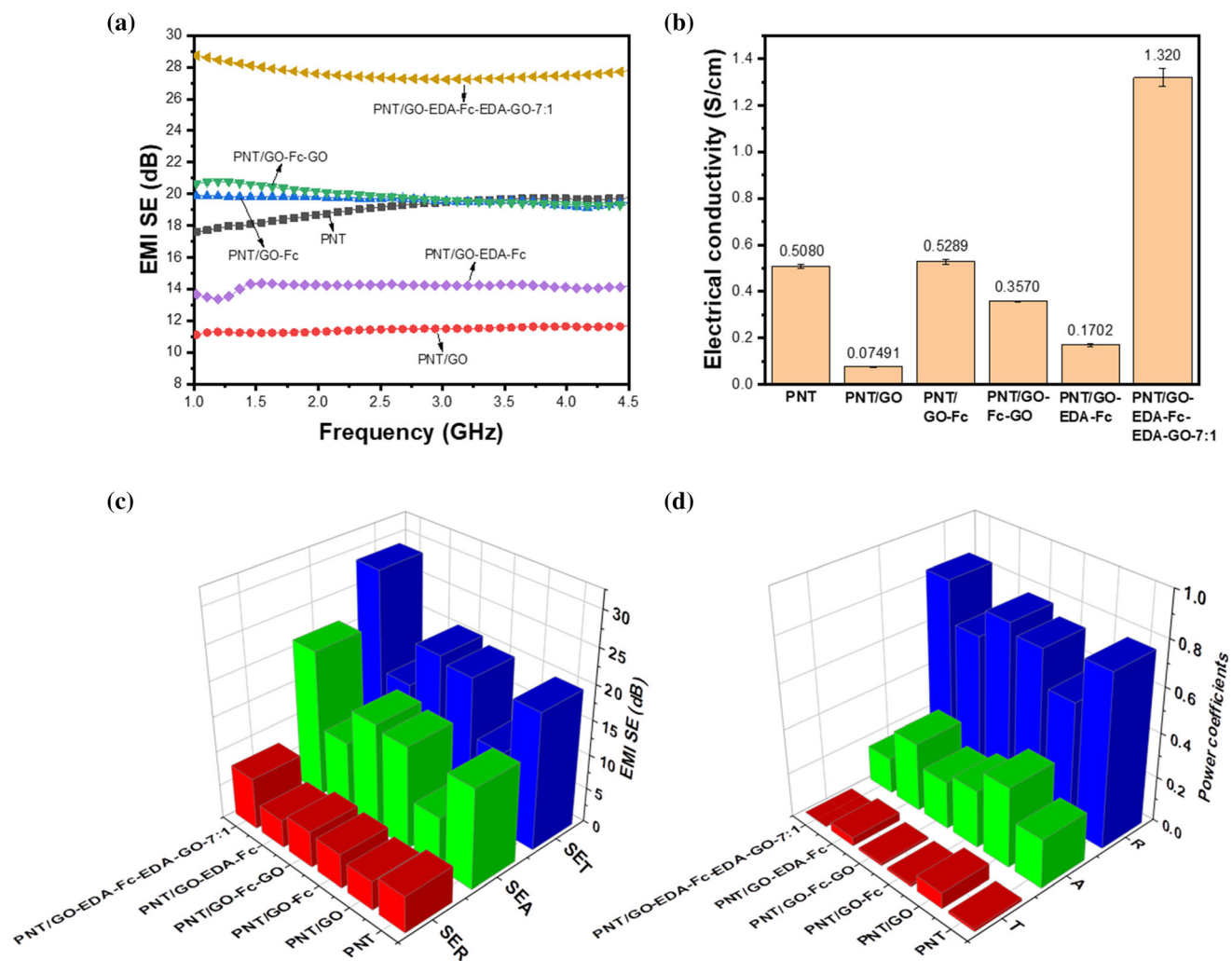
Figure 10 The **a** EMI SE, **b** conductivity, **c** SE_T, SE_A, SE_R and **d** A, R, T of PNT, PNT/GO, PNT/GO-Fc, PNT/GO-Fc-GO, PNT/GO-EDA-Fc and PNT/GO-EDA-Fc-EDA-GO-7:1.

Table 7 Experimental details for the preparation of different fraction ratios of GO-EDA-Fc-EDA-GO in PNT/GO-EDA-Fc-EDA-GO samples

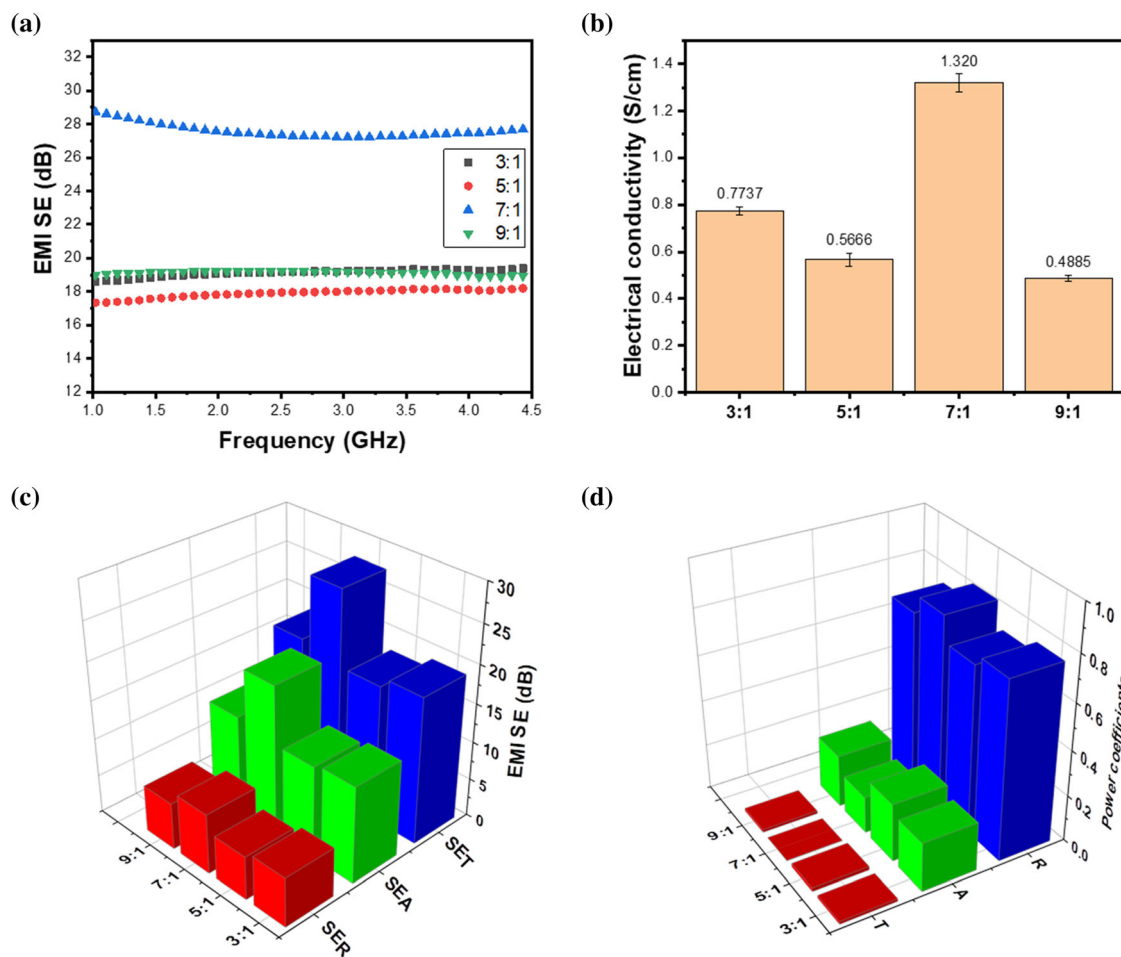| Sample	Step 1		Step 2			Step 3	Time	Temperature
	MO g/mmol	DI water mL	FeCl$_3$·6H$_2$O g/mmol	GO-EDA-Fc-EDA-GO g	t_{stir} h	Py mL/ mmol	h	°C
PNT/GO-EDA-Fc-EDA-GO-3:1	0.3276/1.0	200	2.7078/10.0	0.2338	0.5	0.7/10.1	24	25
PNT/GO-EDA-Fc-EDA-GO-5:1	0.3278/1.0	200	2.7058/10.0	0.1400	0.5	0.7/10.1	24	25
PNT/GO-EDA-Fc-EDA-GO-7:1	0.3272/1.0	200	2.7067/10.0	0.1008	0.5	0.7/10.1	24	25
PNT/GO-EDA-Fc-EDA-GO-9:1	0.3278/1.0	200	2.7086/10.0	0.0781	0.5	0.7/10.1	24	25

Figure 11 The **a** EMI SE, **b** conductivity, **c** SE_T, SE_A, SE_R and **d** A, R, T of different fraction ratios of GO-EDA-Fc-EDA-GO in PNT/GO-EDA-Fc-EDA-GO samples.

Fc-EDA-GO-7:1 and PNT/GO- EDA-Fc-EDA-GO-9:1, respectively (abbreviated to 3:1, 5:1, 7:1 and 9:1 in Fig. 11). And PNT/GO-EDA-Fc-EDA-GO-7:1 is the same sample in Table 5.

Figure 11 illustrates the EMI SE, conductivity, SE_T, SE_A, SE_R, A, R and T graphs of different fraction ratios of GO-EDA-Fc-EDA-GO in PNT/GO-EDA-Fc-EDA-GO samples. As can be seen from Fig. 11a, with the increase of the feed ratio between pyrrole and GO-EDA-Fc-EDA-GO, the EMI SE value also increased, which may be related to whether the GO-EDA-Fc-EDA-GO was uniformly dispersed in the composite material. When the feed ratio increased to 7:1, its EMI SE reached the highest of 28.73 dB. However, when the feed ratio was further increased, that is, when the addition amount of GO-EDA-Fc-

EDA-GO was further reduced, the EMI SE value of composite decreased significantly. This may be due to the fact that when the content of carbon materials was too small, more heterogeneous interfaces and conductive network pathways could not be formed between PNT and carbon materials, thus affecting the EMI SE value of composite. Figure 11b shows a histogram of the conductivity of samples (the detailed data are listed in Table 8) with different feeding ratios. It can be observed that the conductivities of the samples of PNT/GO-EDA-Fc-EDA-GO-3:1, PNT/GO-EDA-Fc-EDA-GO-5:1 and PNT/GO-EDA-Fc-EDA-GO-9:1 were not much different, which were 0.7737 S/cm, 0.5666 S/cm and 0.4885 S/cm, respectively, while the conductivity of the PNT/GO-EDA-Fc-EDA-GO-7:1 sample was 1.320 S/m, the highest

Table 8 Summary of conductivity values for different fraction ratios of GO-EDA-Fc-EDA-GO in PNT/GO-EDA-Fc-EDA-GO samples

Sample	Conductivity (S/cm)				Standard deviation
	1	2	3	Mean	
PNT/GO-EDA-Fc-EDA-GO-3:1	7.916×10^{-1}	7.551×10^{-1}	7.743×10^{-1}	7.737×10^{-1}	1.826×10^{-2}
PNT/GO-EDA-Fc-EDA-GO-5:1	5.584×10^{-1}	5.983×10^{-1}	5.432×10^{-1}	5.666×10^{-1}	2.846×10^{-2}
PNT/GO-EDA-Fc-EDA-GO-7:1	1.329×10^{0}	1.277×10^{0}	1.354×10^{0}	1.320×10^{0}	3.904×10^{-2}
PNT/GO-EDA-Fc-EDA-GO-9:1	5.018×10^{-1}	4.871×10^{-1}	4.765×10^{-1}	4.885×10^{-1}	1.271×10^{-2}

among all samples, which is also consistent with the analysis results in Fig. 11a. It can be seen from Fig. 11c that the SE_A value of each sample was greater than its SE_R value, which means that the EM waves entering the shielding material were mainly absorption loss. Among them, the PNT/GO-EDA-Fc-EDA-GO-7:1 sample has the highest SE_T value due to the highest SE_A value. The information that can be obtained from Fig. 11d is that the values of R of all samples were greater than the values of A, and the values of T were also negligible. This was because the high-conductivity composite material PNT/GO-EDA-Fc-EDA-GO caused the impedance mismatch between the shielding material and the air, so that EM waves were mainly reflected on the surface of the shielding material.

Figure 12 illustrates the possible EMI shielding mechanism of PNT/modified GO composites. Generally speaking, surface reflection, transmission and dissipation of incident EM waves will occur when they pass through EMI shielding materials. Conductive loss, magnetic loss, interfacial polarization, dipole polarization and internal multiple reflections are the five main EMI shielding mechanisms of these composite materials. First of all, the good conductive network paths were formed between the conductive polymer PNT and modified GO, which provided the possibility for the rapid transfer of electrons, and further led to the enhancement of conductive loss. Secondly, a large number of poles and dipoles existed in doped PNT, resulting in polarization loss, which could further dissipate EM waves. The large amount of heterogeneous interfacial polarization between the conductive polymer and the modified carbon materials could also effectively dissipate EM waves. The diamagnetism produced by ferrocene groups under the action of EM wave could also provide the magnetic loss of materials to a certain extent. The multiple reflections of EM waves inside the composite material, especially the unique hollow structure of PNT, made the EM waves further converted into thermal energy. Therefore, these composites have potential application value in EMI shielding field.

Conclusions

In conclusion, the composites of PNT/GO, PNT/GO-Fc, PNT/GO-Fc-GO, PNT/GO-EDA-Fc and PNT/GO-EDA-Fc-EDA-GO were fabricated via *in situ* chemical oxidative polymerization. The EMI shielding performance of polypyrrole nanotube/ferrocene-modified graphene oxide composites was conducted over the frequency range of 1.0–4.5 GHz. The results showed that when 50 wt% of the PNT/GO-EDA-Fc-EDA-GO-7:1 composite material was added to the paraffin matrix, the SE_T reached 28.73 dB, and the conductivity of PNT/GO-EDA-Fc-EDA-GO-7:1 was 1.320 S/cm; this might be due to the large and stable π–π stacking system formed by GO-EDA-Fc-EDA-GO, and the interactions between PNT and GO-EDA-Fc-EDA-GO such as π–π stacking, hydrogen bonding and electrostatic force, which enhanced the electronic transition ability, thus speeding up the transmission of electrons in the composite material. Meanwhile, the interface polarization between the dipole polarization and the heterogeneous interface further improved the EMI shielding performance of the composite material. In summary, the prepared PNT/GO-EDA-Fc-EDA-GO-7:1 composite material has good application value in the field of EMI shielding.
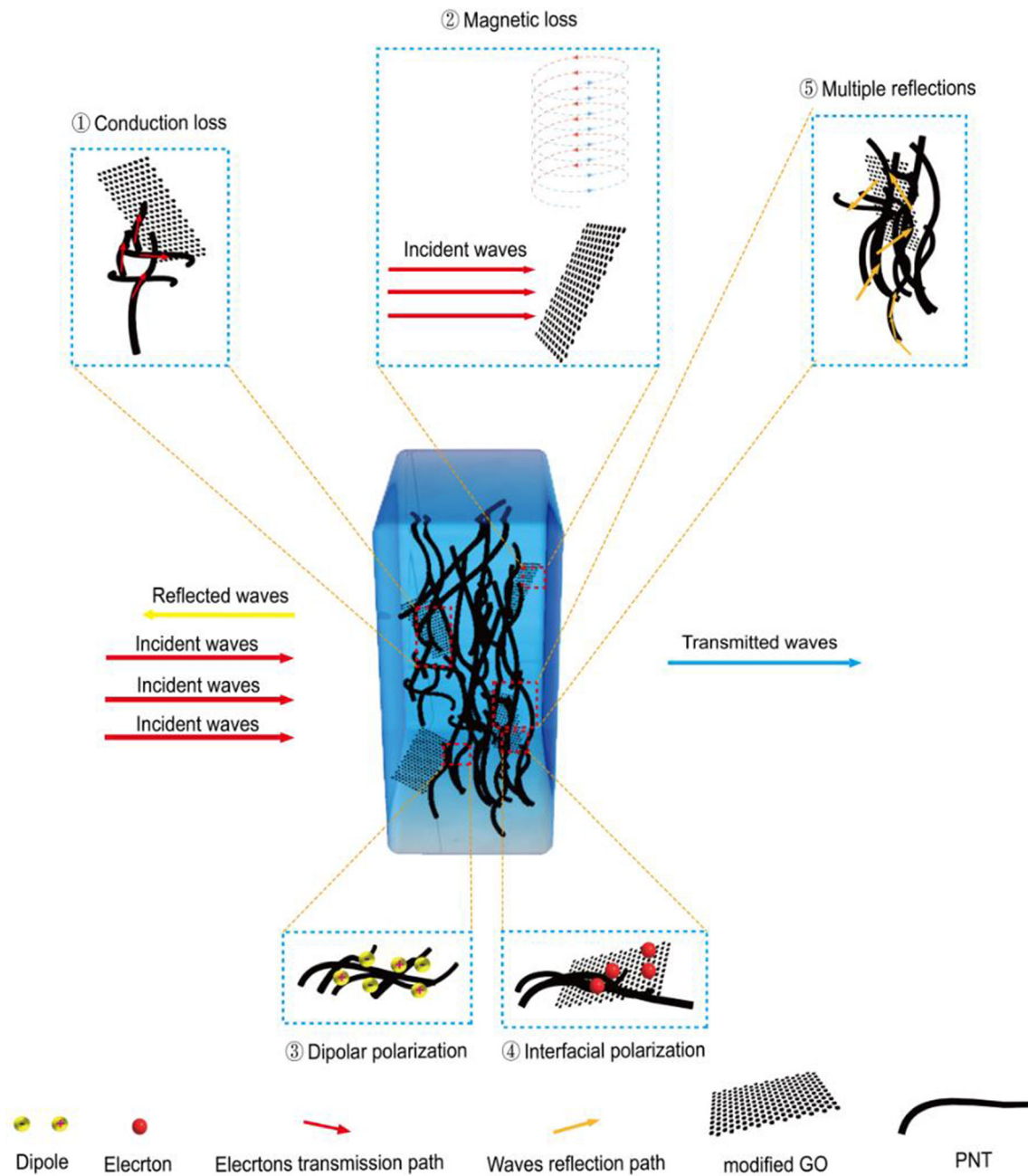
Figure 12 Schematic diagram of possible EMI shielding mechanisms of PNT/modified GO composites.

Declarations

Conflict of interest The authors declare that they have no known competing financial interests or personal relationships that could have appeared to influence the work reported in this paper.

Supplementary Information: The online version contains supplementary material available at http s://doi.org/10.1007/s10853-021-06406-y.

References

[1] Zhang Y, Huang Y, Zhang T, Chang H, Xiao P, Chen H, Huang Z, Chen Y (2015) Broadband and tunable high-performance microwave absorption of an ultralight and highly compressible graphene foam. Adv Mater 27(12):2049–2053. https://doi.org/10.1002/adma.201405788

[2] Wang L, Huang Y, Sun X, Huang H, Liu P, Zong M, Wang Y (2014) Synthesis and microwave absorption enhancement of graphene@Fe_3O_4@SiO_2@NiO nanosheet hierarchical structures. Nanoscale 6(6):3157–3164. https://doi.org/10.10 39/c3nr05313j

[3] Namai A, Sakurai S, Nakajima M, Suemoto T, Matsumoto K, Goto M, Sasaki S, Ohkoshi S-i (2009) Synthesis of an electromagnetic wave absorber for high-speed wireless communication. J Am Chem Soc 131(3):1170–1173. http s://doi.org/10.1021/ja807943v

[4] Huang L, Chen C, Li Z, Zhang Y, Zhang H, Lu J, Ruan S, Zeng Y-J (2020) Challenges and future perspectives on microwave absorption based on two-dimensional materials and structures. Nanotechnology 31(16):162001. https://doi. org/10.1088/1361-6528/ab50af

[5] Yin XW, Kong L, Zhang LT, Cheng LF, Travitzky N, Greil P (2014) Electromagnetic properties of Si-C-N based ceramics and composites. Int Mater Rev 59(6):326–355. https://doi. org/10.1179/1743280414y.0000000037

[6] Li F, Zhan W, Su Y, Siyal SH, Bai G, Xiao W, Zhou A, Sui G, Yang X (2020) Achieving excellent electromagnetic wave absorption of $ZnFe_2O_4$@CNT/polyvinylidene fluoride flexible composite membranes by adjusting processing conditions. Compos Part A-Appl Sci Manuf 133:105866. https://d oi.org/10.1016/j.compositesa.2020.105866

[7] Lin T, Yu H, Wang L, Fahad S, Khan A, K-u-R N, Haq F, Nazir A, Amin BU (2021) A review of recent advances in the preparation of polyaniline-based composites and their electromagnetic absorption properties. J Mater Sci 56(9):5449–5478. https://doi.org/10.1007/s10853-020-0563 1-1

[8] Liu Y, Yin P, Chen J, Cui B, Zhang C, Wu F (2020) Conducting polymer-based composite materials for therapeutic implantations: from advanced drug delivery system to minimally invasive electronics. Int J Polymer Sci 2020:5659682. https://doi.org/10.1155/2020/5659682

[9] Tiwari SK, Mishra J, Hatui G, Nayak GC (2017) Conductive polymer composites based on carbon nanomaterials. Conducting Polymer Hybrids. https://doi.org/10.1007/978-3-319-46458-9_4

[10] Liu JY, Wang JJ, Yu XH, Li L, Shang SM (2015) One-pot synthesis of polypyrrole/AgCl composite nanotubes and their antibacterial properties. Micro & Nano Letters 10(1):50–53. https://doi.org/10.1049/mnl.2014.0435

[11] Qian X, Chen J, An X (2010) Polypyrrole-coated conductive paper prepared by vapour-phase deposition method. Appita J 63(2):102–107

[12] Park K-S, Schougaard SB, Goodenough JB (2007) Conducting-polymer/iron-redox-couple composite cathodes for lithium secondary batteries. Adv Mater 19(6):848–851. htt ps://doi.org/10.1002/adma.200600369

[13] Chen Z, Yu D, Xiong W, Liu P, Liu Y, Dai L (2014) Graphene-based nanowire supercapacitors. Langmuir 30(12):3567–3571. https://doi.org/10.1021/la500299s

[14] Li M, Li H, Zhong W, Zhao Q, Wang D (2014) Stretchable conductive polypyrrole/polyurethane (PPy/PU) strain sensor with netlike microcracks for human breath detection. ACS Appl Mater Interfaces 6(2):1313–1319. https://doi.org/10.1 021/am4053305

[15] Nautiyal A, Qiao M, Cook JE, Zhang X, Huang T-S (2018) High performance polypyrrole coating for corrosion protection and biocidal applications. Appl Surf Sci 427:922–930. h ttps://doi.org/10.1016/j.apsusc.2017.08.093

[16] Tang H, Wang J, Yin H, Zhao H, Wang D, Tang Z (2015) Growth of polypyrrole ultrathin films on MoS_2 monolayers as high-performance supercapacitor electrodes. Adv Mater 27(6):1117–1123. https://doi.org/10.1002/adma.201404622

[17] Tian C, Du Y, Xu P, Qiang R, Wang Y, Ding D, Xue J, Ma J, Zhao H, Han X (2015) Constructing uniform core-shell PPy@PANI composites with tunable shell thickness toward enhancement in microwave absorption. ACS Appl Mater Interfaces 7(36):20090–20099. https://doi.org/10.1021/acsa mi.5b05259

[18] Zhan Y, Zhao R, Xiang X, He S, Zhao S, Xue W (2019) Hierarchical core/shell bamboo-like polypyrrole nanofibers/ Fe_3O_4 hybrids with superior microwave absorption performance. Compos Interfaces 26(12):1087–1100. https://doi.or g/10.1080/09276440.2019.1586043

[19] Liu XY, Yang JX, Li XY, Li Q, Xia YJ (2020) Fabrication of polypyrrole (PPy) nanotube electrode for supercapacitors with enhanced electrochemical performance. J Mater Sci-Mater Electron 31(1):581–586. https://doi.org/10.1007/s108 54-019-02562-9

[20] Babayan V, Kazantseva NE, Moucka R, Stejskal J (2017) Electromagnetic shielding of polypyrrole-sawdust composites: polypyrrole globules and nanotubes. Cellulose 24(8):3445–3451. https://doi.org/10.1007/s10570-017-1357-z

[21] Zhao J, Lin JP, Xiao JP, Fan HL (2015) Synthesis and electromagnetic, microwave absorbing properties of polyaniline/graphene oxide/Fe$_3$O$_4$ nanocomposites. RSC Adv 5(25):19345–19352. https://doi.org/10.1039/c4ra12186d

[22] Chen XN, Chen JJ, Meng FB, Shan LM, Jiang M, Xu XL, Lu J, Wang Y, Zhou ZW (2016) Hierarchical composites of polypyrrole/graphene oxide synthesized by in situ intercalation polymerization for high efficiency and broadband responses of electromagnetic absorption. Compos Sci Technol 127:71–78. https://doi.org/10.1016/j.compscitech.2016.02.033

[23] Bertolini MC, Ramoa S, Merlini C, Barra GMO, Soares BG, Pegoretti A (2020) Hybrid composites based on thermoplastic polyurethane with a mixture of carbon nanotubes and carbon black modified with polypyrrole for electromagnetic shielding. Front Mater 7:174. https://doi.org/10.3389/fmats.2020.00174

[24] Wang Y-Y, Sun W-J, Lin H, Gao P-P, Gao J-F, Dai K, Yan D-X, Li Z-M (2020) Steric stabilizer-based promotion of uniform polyaniline shell for enhanced electromagnetic wave absorption of carbon nanotube/polyaniline hybrids. Composites Part B-Eng 7:199. https://doi.org/10.1016/j.compositesb.2020.108309

[25] Feng D, Xu D, Wang Q, Liu P (2019) Highly stretchable electromagnetic interference (EMI) shielding segregated polyurethane/carbon nanotube composites fabricated by microwave selective sintering. J Mater Chem C 7(26):7938–7946. https://doi.org/10.1039/c9tc02311a

[26] Feng D, Liu PJ, Wang Q (2020) Carbon nanotubes in microwave-assisted foaming and sinter molding of high performance polyetherimide bead foam products. Mater Sci Eng B-Adv Functional Solid-State Mater 262:10. https://doi.org/10.1016/j.mseb.2020.114727

[27] Hu T, Mei X, Wang Y, Weng X, Liang R, Wei M (2019) Two-dimensional nanomaterials: fascinating materials in biomedical field. Sci Bull 64(22):1707–1727. https://doi.org/10.1016/j.scib.2019.09.021

[28] Cui R-B, Zhang C, Zhang J-Y, Xue W, Hou Z-L (2020) Highly dispersive GO-based supramolecular absorber: chemical-reduction optimization for impedance matching. J Alloy Compd 834:155122. https://doi.org/10.1016/j.jallcom.2020.155122

[29] Teimuri-Mofrad R, Abbasi H, Hadi R (2019) Graphene oxide-grafted ferrocene moiety via ring opening polymerization (ROP) as a supercapacitor electrode material. Polymer 167:138–145. https://doi.org/10.1016/j.polymer.2019.01.084

[30] Yang X, Niu X, Mo Z, Liu N, Guo R, Zhao P, Liu Z, Ouyang M (2019) The synthesis of chitosan decorated reduced graphene oxide-ferrocene nanocomposite and its application in electrochemical detection Rhodamine B. Electroanalysis 31(8):1438–1445. https://doi.org/10.1002/elan.201800880

[31] Qiu JD, Deng MQ, Liang RP, Xiong M (2008) Ferrocene-modified multiwalled carbon nanotubes as building block for construction of reagentless enzyme-based biosensors. Sens Actuators B-Chem 135(1):181–187. https://doi.org/10.1016/j.snb.2008.08.017

[32] Karthick NA, Thangappan R, Arivanandhan M, Gnanamani A, Jayavel R (2018) A facile synthesis of ferrocene functionalized graphene oxide nanocomposite for electrochemical sensing of lead. J Inorg Organomet Polym Mater 28(3):1021–1028. https://doi.org/10.1007/s10904-017-0744-0

[33] Gao Y, Hu G, Zhang W, Ma D, Bao X (2011) pi-pi Interaction intercalation of layered carbon materials with metallocene. Dalton Trans 40(17):4542–4547. https://doi.org/10.1039/c0dt01392g

[34] Rabti A, Mayorga-Martinez CC, Baptista-Pires L, Raouafi N, Merkoci A (2016) Ferrocene-functionalized graphene electrode for biosensing applications. Anal Chim Acta 926:28–35. https://doi.org/10.1016/j.aca.2016.04.010

[35] Jin C, Lee J, Lee E, Hwang E, Lee H (2012) Nonvolatile resistive memory of ferrocene covalently bonded to reduced graphene oxide. Chem Commun 48(35):4235–4237. https://doi.org/10.1039/c2cc30973d

[36] Zhou LW L, Yu HJ, Gao JM, Ding WB, Gao HQ (2013) Ferrocene covalently functionalized graphene oxide: Preparation, characterization and catalytic performance for thermal decomposition of ammonium perchlorate. J Mater Sci Eng 31(3):323–330

[37] Saleem M, Wang L, Yu HJ, Zain-ul A, Akram M, Ullah RS (2017) Synthesis of amphiphilic block copolymers containing ferrocene-boronic acid and their micellization, redox-responsive properties and glucose sensing. Colloid Polymer Sci 295(6):995–1006. https://doi.org/10.1007/s00396-017-4049-1

[38] Yang H, Shan C, Li F, Han D, Zhang Q, Niu L (2009) Covalent functionalization of polydisperse chemically-converted graphene sheets with amine-terminated ionic liquid. Chem Commun 26:3880–3882. https://doi.org/10.1039/b905085j

[39] Saleem M, Yu H, Wang L, Zain-ul A, Khalid H, Akram M, Abbasi NM, Chen Y (2016) Study on synthesis of ferrocene-based boronic acid derivatives and their saccharides sensing properties. J Electroanal Chem 763:71–78. https://doi.org/10.1016/j.jelechem.2015.12.028

[40] Yang R-B, Reddy PM, Chang C-J, Chen P-A, Chen J-K, Chang C-C (2016) Synthesis and characterization of Fe$_3$O$_4$/polypyrrole/carbon nanotube composites with tunable

microwave absorption properties: role of carbon nanotube and polypyrrole content. Chem Eng J 285:497–507. https://doi.org/10.1016/j.cej.2015.10.031

[41] Guan LH, Shi ZJ, Li MX, Gu ZN (2005) Ferrocene-filled single-walled carbon nanotubes. Carbon 43(13):2780–2785. https://doi.org/10.1016/j.carbon.2005.05.025

[42] Amer WA, Wang L, Amin AM, Yu HJ, Li C, Ma L (2013) Study on the electrochemical, thermal, and liquid crystalline properties of poly(diethyleneglycol 1,1 '-ferrocene dicarboxylate). Des Monomers Polym 16(2):160–169. https://doi.org/10.1080/15685551.2012.705504

[43] Sangeetha V, Kanagathara N, Sumathi R, Sivakumar N, Anbalagan G (2013) Spectral and thermal degradation of melamine cyanurate. J Mater 2013:1–7

[44] Larkin PJ, Makowski MP, Colthup NB, Flood LA (1998) Vibrational analysis of some important group frequencies of melamine derivatives containing methoxymethyl, and carbamate substituents: mechanical coupling of substituent vibrations with triazine ring modes. Vib Spectrosc 17(1):53–72. https://doi.org/10.1016/s0924-2031(98)00015-0

[45] Jing HY, Ren SZ, Shi YT, Song XD, Yang Y, Guo YN, An YL, Hao C (2017) Ozonization, amination and photoreduction of graphene oxide for triiodide reduction reaction: an experimental and theoretical study. Electrochim Acta 226:10–17. https://doi.org/10.1016/j.electacta.2016.12.190

[46] Wu L, Lu X, Dhanjai W-S, Dong Y, Wang X, Zheng S, Chen J (2018) 2D transition metal carbide MXene as a robust biosensing platform for enzyme immobilization and ultrasensitive detection of phenol. Biosens Bioelectron 107:69–75. https://doi.org/10.1016/j.bios.2018.02.021

[47] Krishnamoorthy K, Veerapandian M, Yun K, Kim SJ (2013) The chemical and structural analysis of graphene oxide with different degrees of oxidation. Carbon 53:38–49. https://doi.org/10.1016/j.carbon.2012.10.013

[48] Marcano DC, Kosynkin DV, Berlin JM, Sinitskii A, Sun ZZ, Slesarev A, Alemany LB, Lu W, Tour JM (2010) Improved synthesis of graphene oxide. ACS Nano 4(8):4806–4814. https://doi.org/10.1021/nn1006368

[49] Cao N, Zhang Y (2015) Study of reduced graphene oxide preparation by Hummers' method and related characterization. J Nanomater 2015:168125. https://doi.org/10.1155/2015/168125

[50] Shen JF, Hu YZ, Shi M, Lu X, Qin C, Li C, Ye MX (2009) Fast and facile preparation of graphene oxide and reduced graphene oxide nanoplatelets. Chem Mater 21(15):3514–3520. https://doi.org/10.1021/cm901247t

[51] Stankovich S, Dikin DA, Piner RD, Kohlhaas KA, Kleinhammes A, Jia Y, Wu Y, Nguyen ST, Ruoff RS (2007) Synthesis of graphene-based nanosheets via chemical

reduction of exfoliated graphite oxide. Carbon 45(7):1558–1565. https://doi.org/10.1016/j.carbon.2007.02.034

[52] Kudin KN, Ozbas B, Schniepp HC, Prud'homme RK, Aksay IA, Car R (2008) Raman spectra of graphite oxide and functionalized graphene sheets. Nano Lett 8(1):36–41. https://doi.org/10.1021/nl071822y

[53] Li YT, Lian HQ, Hu YN, Chang W, Cui XG, Liu Y (2016) Enhancement in mechanical and shape memory properties for liquid crystalline polyurethane strengthened by graphene oxide. Polymers 8(7):236. https://doi.org/10.3390/polym8070236

[54] Avinash MB, Subrahmanyam KS, Sundarayya Y, Govindaraju T (2010) Covalent modification and exfoliation of graphene oxide using ferrocene. Nanoscale 2(9):1762–1766. https://doi.org/10.1039/c0nr00024h

[55] Lu YZ, Jiang YY, Wu HB, Chen W (2015) Ferrocene-functionalized graphene oxide nanosheets: efficient electronic communication between ferrocene centers across graphene nanosheets. Electrochim Acta 156:267–273. https://doi.org/10.1016/j.electacta.2015.01.049

[56] Kosowska K, Domalik-Pyzik P, Sekula-Stryjewska M, Noga S, Jagiello J, Baran M, Lipinska L, Zuba-Surma E, Chlopek J (2020) Gradient chitosan hydrogels modified with graphene derivatives and hydroxyapatite: physiochemical properties and initial cytocompatibility evaluation. Int J Mol Sci 21(14):4888. https://doi.org/10.3390/ijms21144888

[57] Al-Gaashani R, Najjar A, Zakaria Y, Mansour S, Atieh MA (2019) XPS and structural studies of high quality graphene oxide and reduced graphene oxide prepared by different chemical oxidation methods. Ceram Int 45(11):14439–14448. https://doi.org/10.1016/j.ceramint.2019.04.165

[58] Yamada Y, Kim J, Matsuo S, Sato S (2014) Nitrogen-containing graphene analyzed by X-ray photoelectron spectroscopy. Carbon 70:59–74. https://doi.org/10.1016/j.carbon.2013.12.061

[59] Li B, Wu WB, Zhang TY, Jiang S, Chen XW, Zhang GH, Zhang X (2017) Ferrocene particles incorporated into Zr-based metal-organic frameworks for selective phenol hydroxylation to dihydroxybenzenes. RSC Adv 7(61):38691–38698. https://doi.org/10.1039/c7ra06917k

[60] Wu J, Dai Y, Pan Z, Huo D, Wang T, Zhang H, Hu J, Yan S (2020) Co_3O_4 hollow microspheres on polypyrrole nanotubes network enabling long-term cyclability sulfur cathode. Appl Surf Sci 510:145529. https://doi.org/10.1016/j.apsusc.2020.145529

[61] Liu Y, Wang Y, Chen Y, Wang C, Guo L (2020) NiCo-MOF nanosheets wrapping polypyrrole nanotubes for high-

performance supercapacitors. Appl Surf Sci 507:145089. https://doi.org/10.1016/j.apsusc.2019.145089

[62] Cao G, Wang L, Tian Y (2020) Highly dispersed polypyrrole nanotubes for improving the conductivity of electrically conductive adhesives. J Mater Sci-Mater Electron 31(12):9675–9684. https://doi.org/10.1007/s10854-020-03513-5

[63] Tian K, Su Z, Wang H, Tian X, Huang W, Xiao C (2017) N-doped reduced graphene oxide/waterborne polyurethane composites prepared by in situ chemical reduction of graphene oxide. Compos Part A-Appl Sci Manuf 94:41–49. https://doi.org/10.1016/j.compositesa.2016.11.020

[64] Wang Y, Guan H, Dong C, Xiao X, Du S, Wang Y (2016) Reduced graphene oxide (RGO)/Mn$_3$O$_4$ nanocomposites for dielectric loss properties and electromagnetic interference shielding effectiveness at high frequency. Ceram Int 42(1):936–942. https://doi.org/10.1016/j.ceramint.2015.09.022

[65] Li Q, Chen L, Ding J, Zhang J, Li X, Zheng K, Zhang X, Tian X (2016) Open-cell phenolic carbon foam and electromagnetic interference shielding properties. Carbon 104:90–105. https://doi.org/10.1016/j.carbon.2016.03.055

[66] Sheng A, Ren W, Yang Y, Yan D-X, Duan H, Zhao G, Liu Y, Li Z-M (2020) Multilayer WPU conductive composites with controllable electro-magnetic gradient for absorption-dominated electromagnetic interference shielding. Composites Part a-Appl Sci Manufacturing 129:105692. https://doi.org/10.1016/j.compositesa.2019.105692

[67] Lin T, Yu H, Wang L, Ma Q, Huang H, Wang L, Uddin MA, Haq F, Lemenovskiy DA (2021) A study on the fabrication and microwave shielding properties of PANI/C-60

heterostructures. Polym Compos 42:1961–1976. https://doi.org/10.1002/pc.25948

[68] Al-Saleh MH, Sundararaj U (2009) Electromagnetic interference shielding mechanisms of CNT/polymer composites. Carbon 47(7):1738–1746. https://doi.org/10.1016/j.carbon.2009.02.030

[69] Karim MR, Hatakeyama K, Matsui T, Takehira H, Taniguchi T, Koinuma M, Matsumoto Y, Akutagawa T, Nakamura T, Noro S, Yamada T, Kitagawa H, Hayami S (2013) Graphene oxide nanosheet with high proton conductivity. J Am Chem Soc 135(22):8097–8100. https://doi.org/10.1021/ja401060q

[70] Liu J, Zhang H-B, Sun R, Liu Y, Liu Z, Zhou A, Yu Z-Z (2017) Hydrophobic, flexible, and lightweight MXene foams for high-performance electromagnetic-interference shielding. Adv Mater 29(38):1702367. https://doi.org/10.1002/adma.201702367

[71] Mei X, Lu L, Xie Y, Wang W, Tang Y, Teh KS (2019) An ultra-thin carbon-fabric/graphene/poly(vinylidene fluoride) film for enhanced electromagnetic interference shielding. Nanoscale 11(28):13587–13599. https://doi.org/10.1039/c9nr03603b

[72] Mei X, Lu L, Xie Y, Yu Y-X, Tang Y, Teh KS (2020) Preparation of flexible carbon fiber fabrics with adjustable surface wettability for high-efficiency electromagnetic interference shielding. ACS Appl Mater Interfaces 12(43):49030–49041. https://doi.org/10.1021/acsami.0c08868

Publisher's Note Springer Nature remains neutral with regard to jurisdictional claims in published maps and institutional affiliations.